Technical Note: Analysis of concentration-discharge hysteresis loops using Self-Organizing Maps

Arlex Marin-Ramirez, David Tyler Mahoney, Grace McDaniel

Dept. of Civil and Environmental Engineering, University of Louisville, Louisville, KY, 40208, USA

Correspondence to: Tyler Mahoney (tyler.mahoney@louisville.edu)

Abstract. Analyzing concentration–discharge (C–Q) hysteresis loops is essential for understanding both dissolved and particulate constituent sources and transport mechanisms in watershed hydrology. However, traditional hysteresis analysis methods, including loop classification schemes and hysteresis indices, fail to capture the full variability and gradual transitions between loop patterns. To address these limitations, we introduce an alternative approach for characterizing hysteresis patterns in watersheds using the Self-Organizing Map (SOM) algorithm, which better represents loop variability without relying on rigid categories. This technical ~~report~~ note outlines the application–and the advantages–of SOM-based hysteresis loop characterization and presents a general workflow for its implementation to characterize C-Q hysteresis for any watershed constituent. We demonstrate the efficacy of the SOM algorithm through a proof-of-concept with sediment transport hysteresis loops. The SOM algorithm was able to classify hysteresis loops with a high degree of accuracy, correctly mapping the amplitude, direction, and concavity of hysteresis loops in the training dataset. We also used the SOM algorithm to develop a *General Turbidity-Discharge (T-Q) SOM*—which may be used as a standard~~ized benchmark classification model~~ for characterizing primary loop types in sediment hysteresis analysis. We demonstrate the use of the *General T-Q SOM* in describing loop frequency distributions and exploring associations with hydrologic variables to infer hydrologic controls of loop types ~~for three watersheds~~. We found that the *General T-Q SOM* captures key differences in loop shape (and thus sediment transport processes) overlooked by hysteresis indices while preserving the ~~continuum of loop variability~~ gradual transitions between loop types that are often lost in classification schemes. Additionally, SOM-based correlation analysis effectively detected associations between loop types and hydrologic variables, enhancing understanding of their hydrologic significance. ~~Combined with high-resolution water quality data, t~~This method offers a powerful tool for advancing the identification of constituent sources and transport mechanisms at the watershed scale. To support broader adoption of the methodology described in this paper, we have developed a Python package, equipped with detailed documentation, to facilitate SOM implementation and application in future C-Q analysis.

1 Introduction

The analysis of event-scale concentration–discharge (C-Q) hysteresis loops has been employed for decades to infer mechanisms governing the export of dissolved and particulate constituents from watersheds (Heidel, 1956; Williams, 1989; Evans and Davies, 1998; Malutta et al., 2020; Liu et al., 2021; Mazilamani et al., 2024; Speir et al., 2024; Jing et al., 2025). These hysteretic patterns are commonly used to characterize time lag~~s~~ between water and constituent export~~s~~, flushing versus ~~diluting behavior~~ dilution during storm events, and the dispersion and skewness of water and constituent pulses (Williams, 1989; Evans and Davies, 1998; Zuecco et al., 2016). Hysteresis analyses have proven valuable for identifying sources of distributed pollutants in watersheds (Williams, 1989; Molder et al., 2015; Pickering and Ford, 2021), understanding pollutant transport pathways (Evans and Davies, 1998; Marin-Ramirez et al., 2024; Bettel et al., 2025), improving model calibration (Husic et al., 2023), assessing the impact of watershed and in-stream alterations such as land use/land cover changes and restoration strategies (Gellis, 2013; Pickering and Ford, 2021; Zarnaghsh and Husic, 2021; Bettel et al., 2025), and supporting

Formatted: Space Before: 0 pt, Line spacing: Multiple 1.15 li

Formatted: Space Before: 0 pt, After: 12 pt, Line spacing: Multiple 1.15 li

Formatted: Space Before: 0 pt, Line spacing: Multiple 1.15 li

Formatted: Line spacing: Multiple 1.15 li

Formatted: Space Before: 0 pt

Formatted: Line spacing: Multiple 1.15 li

better comprehension of catchment functioning to inform management practices (Sherriff et al., 2016; Haddadchi and Hicks, 2021).

Traditionally, the characterization of hysteresis patterns has relied on classification schemes and hysteresis indices (Mazilamani et al., 2024). The former categorizes loops into predefined shapes such as clockwise, counterclockwise, or linear (Williams, 1989), whereas the latter involves representing loops with an index that typically captures information regarding the loop amplitude and direction (e.g., clockwise or counterclockwise) (Lloyd et al., 2016; Zuecco et al., 2016). Both approaches, however, have limitations. Manual classification is time-consuming and impractical for large datasets, which are increasingly common due to high-resolution in-situ monitoring. While this limitation can be overcome with automatic classification methods (*sensu* ~~(~~Hamshaw et al., 2018) ~~Hamshaw et al. (2018))~~, a more fundamental limitation persists: classification schemes impose rigid and subjective boundaries that fail to capture the continuous variation in hysteresis loop patterns (see Fig. 1). These strict boundaries result in poor description of ~~loops~~ similarities and differences between loops, potentially hindering statistical analyses that aim to link loop patterns to their controlling factors.

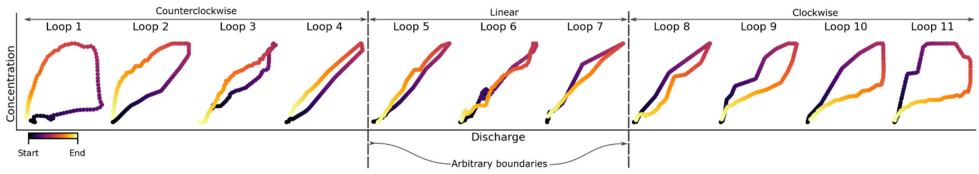

Figure 1. Examples of hysteresis loops arranged to show the smooth transition from wide counterclockwise loops (left), through linear ~~relationships~~ loops (center), to wide clockwise loops (right). The figure demonstrates the limitations of traditional classification schemes which rely on rigid boundaries that fail to account for the gradual transition between loop types. For instance, if loops are classified based on the depicted boundaries, the similarity between loop 4 and loop 5 would not be captured. This classification scheme would, in fact, treat loop 4 and loop 5 as being as categorically distinct as loop 1 and loop 5, despite the clear ~~topological~~ similarities. The depicted hysteresis loops are derived from turbidity and discharge data collected by the USGS across eight different watersheds (see section 3.1.1)

The use of hysteresis indices addresses some of these limitations. They can be automated for large datasets and preserve some of the continuous variability of hysteresis loops. For instance, the indices proposed by Zuecco et al. (2016) and Lloyd et al. (2016)—which are among the most commonly used—range from -1 to 1, reflecting the transition from counterclockwise to clockwise, with zero indicating the absence of a loop (single line).

While the analysis of hysteresis indices has proven effective for revealing information about dominant hydrologic processes in watersheds (Liu et al., 2021; Zarnaghsh and Husic, 2021; Marin-Ramirez et al., 2024), these indices often cannot capture meaningful differences in loop shape. For example, the hysteresis index values (as calculated following ~~(~~Zuecco et al., 2016)~~)~~ of the clockwise loops in Fig. 2 are equal despite presenting significant qualitative differences, not just in the loop shape itself, but in the characteristics of the discharge and concentration pulses. Particularly, Event 1 and Event 2 differ in their concavity (concave-up and concave-down, respectively) which reflects differences in the relative spread of the discharge and concentration pulses (Williams, 1989). As ~~can be seen~~shown in the lower panel of Fig. 2, concave-up loops occur when the concentration pulse is narrower than the discharge pulse, whereas concave-down loops indicate a wide concentration pulse, likely reflecting a persistent source that remains active during the receding limb of the event. Event 3 on the other hand, shows

Formatted: Font: Not Italic

Formatted: Line spacing: Multiple 1.15 li

an extreme case of a leading concentration pulse, where the concentration rises and recedes almost entirely during the rising limb of the hydrograph producing an "L" shaped loop. This loop shape suggests a strong decoupling between stream discharge and concentration. Despite these differences, the hysteresis index of each loop ~~shown~~ in Fig. 2 is identical, ~~thus~~ demonstrating its limitation to capture loop features relevant for distinguishing transport mechanisms and/or sources.

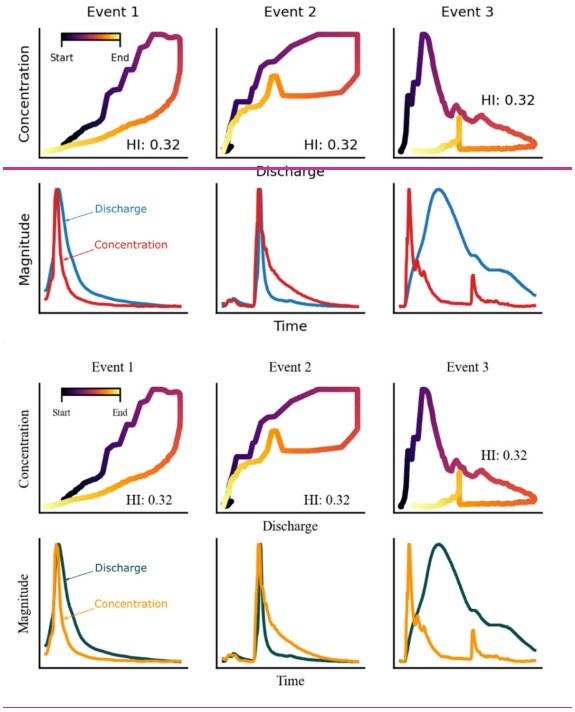

Figure 2. Examples of hydrologic events with hysteresis loops that yield identical hysteresis index values (as defined by ~~(~~Zuecco et al., 2016)~~)~~ despite notable differences in their C-Q relationships. For instance, the variation in concavity between events 1 and 2 reflects differences in the width of the concentration pulse, while the distinctive 'L'-shaped loop in event 3 suggests a decoupling between stream discharge and concentration. These examples illustrate the limitations of hysteresis indices in capturing critical differences in loop shapes that are essential for characterizing transport dynamics. The depicted loops are based on turbidity and discharge data collected by the USGS from three watersheds (see section 3.1.1).

To overcome the limitations of traditional classification schemes and hysteresis indices, we propose characterizing discharge-concentration hysteresis loops using Self-Organizing Maps (SOM). SOM is an unsupervised machine learning algorithm (Kohonen, 1990) widely used for clustering, dimensionality reduction, and data visualization. Although extensively used in water resources ~~analysis~~ (Kalteh et al., 2008; Clark et al., 2020), to our knowledge, its potential for characterizing hysteresis

Formatted: Space Before: 0 pt

Formatted: Line spacing: Multiple 1.15 li

loops has yet to be explored. When applied to C-Q hysteresis loops, SOM generates a two-dimensional map, also called a Kohonen map, that may enable improved representation of loop type variability, deeper exploration of loop characteristics, and enhanced interpretation of diverse C-Q relationships. Furthermore, the algorithm may support key workflows in hysteresis analysis, including data visualization, clustering of similar loop patterns, and correlation analysis to uncover potential controls on loop types, while taking advantage of machine learning's ability to analyze large datasets.

In this technical note, we evaluate the efficacy of the SOM algorithm to represent hysteresis loop patterns and discriminate hysteresis loop types, compared to traditional classification schemes and hysteresis indices. We use a dataset of turbidity (as a proxy for sediment concentration) and discharge to provide a proof-of-concept for using SOM to discriminate and characterize loop types commonly seen in sediment transport literature. In the following sections, we: (i) present a brief description of the SOM algorithm and explain its advantageshow to use it its application for C-Q hysteresis analysis (Section 2), (ii) present a proof-of-concept for the use of SOM to analyze turbidity–discharge hysteresis loops (Section 3 and 4), (iii) compare results from SOM with the hysteresis index and discuss its efficacy in discriminating samples between different loop types (Section 4), and (iv) show how to use the SOM algorithm with data from any watershed (regardless of the number of hysteresis loop samples available) to describe the distribution of loop patterns and explore the association between loop types and their potential controlling factors (Section 4 and 5). Finally, to support broader adoption of the methodology described in this paper, we have developed a Python package, *HySOM*, equipped with detailed documentation to facilitate SOM implementation and application in future C-Q analysis (Section 7).

2 Self-Organizing Maps for C-Q hysteresis analysis

2.1 Brief description of SOM

The SOM algorithm, developed by (Kohonen, 1982; Kohonen, 1990) Kohonen (1982); (Kohonen, 1990), is an unsupervised learning technique widely applied in various fields, including clustering, classification, manifold learning, dimensionality reduction, and data visualization (Miljković, 2017). In water resources, SOM has been applied to for diverse purposes such as rainfall-runoff modelling, regionalization, clustering of water quality data, analysis of land use and land cover, and more (Kalteh et al., 2008; Clark et al., 2020). This The algorithm generates a discrete representation of a dataset known as a feature map or Kohonen map (Miljković, 2017), which typically takes the form of a two-dimensional grid of nodes arranged in either a rectangular or hexagonal lattice. Each of these nodes acts asrepresents a *prototype*, representing a cluster of similar *samples* (, here, a number of individual hysteresis loops) in the training dataset. . Furthermore, tThe spatial arrangement of prototypes on the map preserves the topological structure of the input training data: such that similar prototypes are placed close to each other, while dissimilar prototypes are placed farther apart. In the context of hysteresis, the input samples to the SOM algorithm include are paired sequences of discharge and concentration values data, each of them representing a hysteresis events, and the output of the SOM algorithm is a set of prototype loops that represent characteristic C-Q behavior arranged in a continuum.

Each node in the map has an associated prototype vector that acts as a centroid, representing a cluster of similar samples. Furthermore, the arrangement of prototypes preserves the topological structure of the training data: similar prototypes are placed close to each other, while dissimilar prototypes are placed farther apart. Conventionally, these prototypes are represented as n-dimensional vectors, sharing the same dimensionality as the training samples. However, as explained further below, we represent the hysteresis loops using $n \times 2$ arrays which represent a n-length sequence of (Q, C) data pairs.
In the context of hysteresis analysis, the SOM algorithm can extract representative loops from a dataset and arrange them in a coherent manner, offering a two-dimensional, semi-continuous representation of the dataset's loops. By projecting these loops into a two-dimensional space, SOM retains more information compared to the hysteresis index, which offers only a one-

Formatted: Font: Italic
Formatted: Space Before: 0 pt
Formatted: Space Before: 0 pt, Line spacing: Multiple 1.15 li
Formatted: Line spacing: Multiple 1.15 li
Formatted: Not Highlight
Formatted: Not Highlight
Formatted: Not Highlight
Formatted: Font: Italic
Formatted: Font: Italic
Formatted: Not Highlight
Formatted: Not Highlight
Formatted: Not Highlight
Formatted: Not Highlight
Formatted: Not Highlight
Formatted: Space After: 0 pt, Line spacing: Multiple 1.15

dimensional projection, while maintaining a low dimensionality that enables easier analysis and visualization. For instance, the frequency distribution of loop types can be visualized as a heatmap or scatter plot mapped onto the trained Kohonen map. Additionally, this map can serve as a tool to visualize and quantify the relationships between loop types and their potential hydrologic controls, as demonstrated in Section 4.Each node in the map has an associated prototype vector that acts as a centroid, representing a cluster of similar samples. Furthermore, the arrangement of prototypes preserves the topological structure of the training data: similar prototypes are placed close to each other, while dissimilar prototypes are placed farther apart. Conventionally, these prototypes are represented as n-dimensional vectors, sharing the same dimensionality as the training samples. However, as explained further below, we represent the hysteresis loops using $n \times 2$ arrays which represent a n-length sequence of (Q, C) data pairs.

2.25 AWorkflow for applying SOM forin hysteresis analysis

We propose using SOM for C-Q hysteresis analysis following the two-phase workflow illustrated in Fig. 3. The first phase —tThe *Training phase*— involves constructing an SOM to represent the spectrum of hysteresis loop types associated with a specific dissolved or particulate constituent. To ensure the trained SOM adequately captures the diversity of loop patterns, we recommend curating a training dataset that includes a similar number of representative examples of all known loop types for the constituent under investigation. This curated dataset serves three key purposes: (i) to represent the known hysteresis loops for a given constituent, thereby ensuring broad applicability of the resulting SOM; (ii) to guarantee representation of less frequent patterns; and (iii) to provide a reference for evaluating the SOM's ability to distinguish loops in line with conceptual classifications (last step of the *Training phase*, Fig. 3). More details on the training and evaluation procedures are provided in section 2.5.enables the for a given constituent as well as evaluation of we found in our implementation that

While dataset curation is a time-intensive task, requiring the extraction of multiple hydrologic events (for example, we included 340 events in our proof-of-concept; see Section 3.1), often from several watersheds, it is typically performed only once for each constituent's SOM. Once trained, the SOM can be readily shared and reused by other researchers without the need for retraining. For instance, along with this Technical Note, we released a trained SOM for sediment transport hysteresis analysis—referred to as the *General T–Q SOM*—which is publicly available (section 7) for use in sediment hysteresis analysis studies.

The output of the Training phase first phase is a trained SOM composed of coherently arranged prototypes reflecting the range of loop types in the training dataset. For instance, along with this Ttechnical Nnote, we released a trained SOM for sediment transport hysteresis analysis—referred to as the *General T–Q SOM*—which is publicly available (section 7) for use in sediment hysteresis analysis studies (section 7). Further More

During the training process, an SOM should be selected that provides a coherent arrangement and smooth transition between loop types (i.e., low topographic error) while accurately representing the training data (i.e., low quantization error).

The second phase —tThe *Analysis phase*— of the workflow consists of using the trained SOM to characterizeclassify loop types from any datasetin new datasets, provided (assuming that they correspond are of the to the same constituent of interest). First, Eeach loop in the dataset is mapped to its most similar loop prototype, known as the Best Matching Unit (BMU), based on a a predefined similarity metric or distance function, as described in see section 2.4—. This classification enables systematic analysis of hysteresis patterns across watersheds. For example, Bby quantifying the number of samples assigned to each prototype, researchers can characterize the frequency distribution of loop types and investigate their associations with hydrological variablesto aid with analyzing hysteresis patterns in watersheds. This involves mapping each hysteresis loop in the dataset to its corresponding BMU within the trained SOM. Importantly, this procedure does not require reapplying the SOM algorithm itself; rather, it only requires the distance function to map each sample to its corresponding prototype. As

Formatted: Space Before: 0 pt, Line spacing: Multiple 1.15 li

Formatted: Line spacing: Multiple 1.15 li

Formatted: Strikethrough, Highlight

Formatted: Font: Italic

Formatted: Space After: 12 pt, Line spacing: Multiple 1.15 li

~~demonstrated in our proof-of-concept in section 3, this approach can be employed to characterize the frequency distributions of loop types and explore associations between loop types and hydrological variables~~, thereby providing valuable insights into the underlying controlling mechanisms, as demonstrated in Section 4. ~~We have released a Python package with this Technical Note, called *HySOM*, to aid users with implementation of this workflow (see Section 7).~~

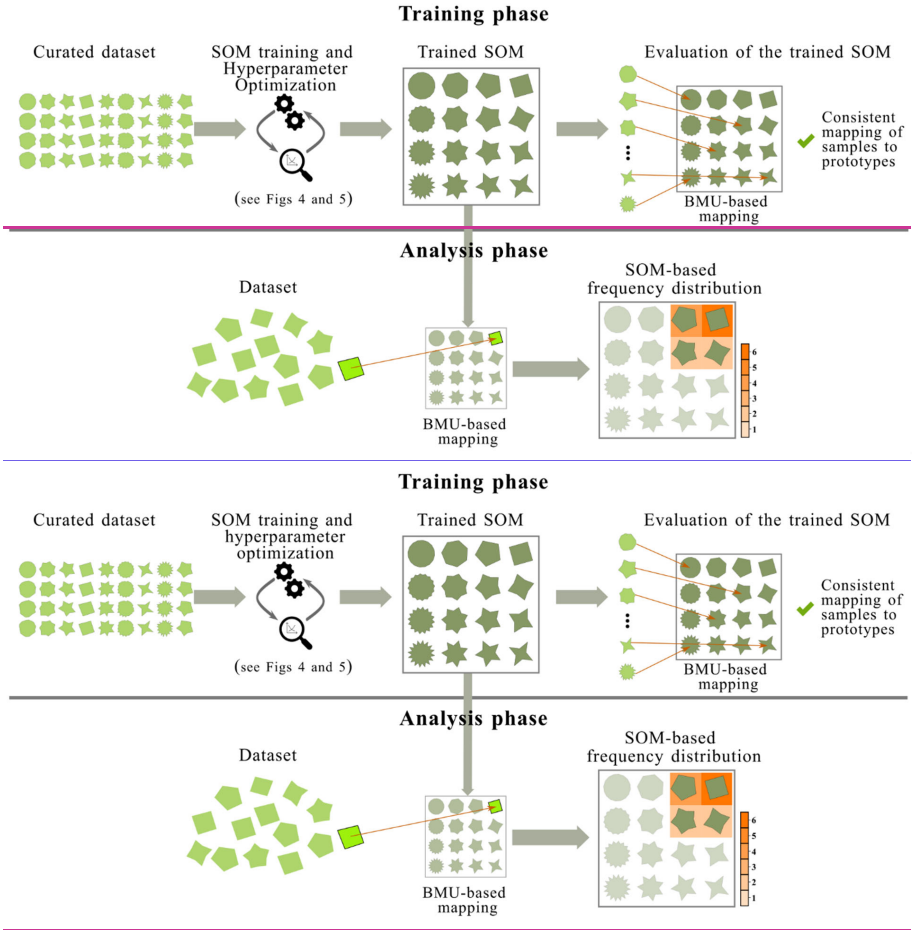

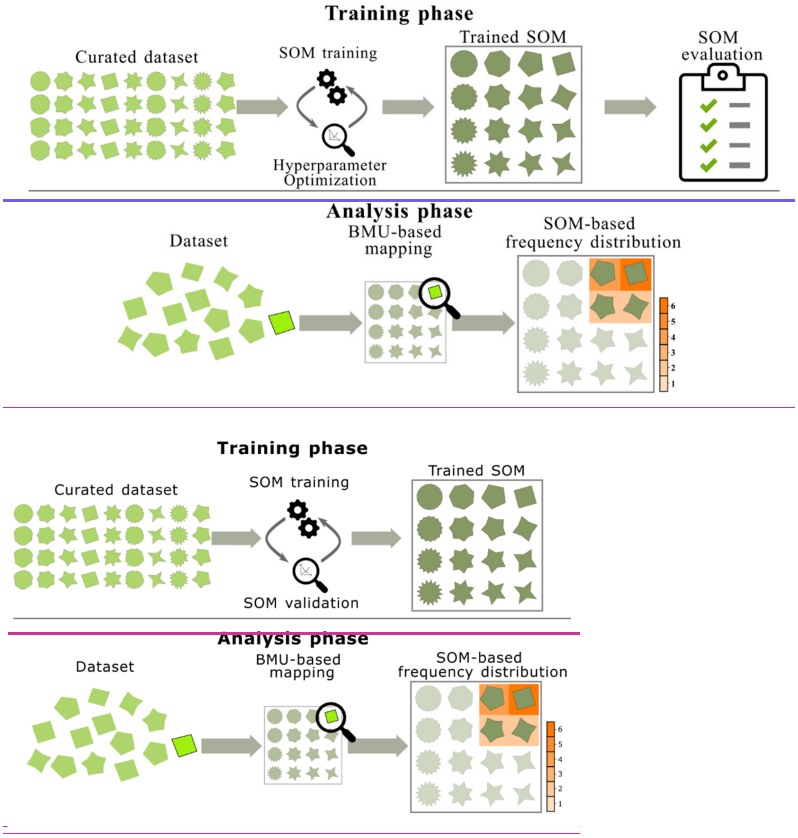

Figure 3. Workflow to generate an SOM for C-Q hysteresis loops (~~t~~*Training phase*) and apply the SOM for C-Q hysteresis analyses in watersheds (~~a~~*Analysis phase*). Here, we illustrate the generation of the SOM using different shapes, which are analogous to the hysteresis loop types that might be found for a dissolved or particulate constituent in a watershed. In the bottom panel (~~a~~*Analysis phase*), we demonstrate how hysteresis loops from a new dataset get mapped to the trained SOM, where the shade of orange represents the frequency with which the shape occurs in the dataset. The *HySOM* python package (see section 7) allows users to implement both phases of this workflow.

2.3 Representing hysteresis loops for SOM

In Fig. 3, samples (in ~~the~~ light green ~~shapes~~) and prototypes (~~the~~ in dark green ~~shapes~~) are depicted as geometric shapes for illustrative purposes. However, ~~to be compatible with SOM,~~the SOM algorithm requires that ~~the~~ input data ~~must~~ be represented

Formatted: Justified, Space After: 12 pt, Line spacing: Multiple 1.15 li

Formatted: Font: Italic

Formatted: Font: Italic

Formatted: Font: Italic

Formatted: Heading 2, Space After: 0 pt, Line spacing: single

Formatted: Line spacing: Multiple 1.15 li

as numeric arrays. In conventional SOM applications, each sample is represented as an n-dimensional vector~~, and likewise,~~ and each resulting prototype is ~~also a~~~~n n – dimensional~~ vector of the same dimension. For C-Q hysteresis analysis, ~~however,~~ we propose representing each loop~~s~~ as a sequence~~s~~ of paired discharge-concentration values, ~~(Q, C) data pairs. Under this representation, each sample (loop) corresponds to an~~ forming a matrix with dimensions $n \times 2$, ~~matrix with~~ where n ~~indicating~~ indicates the number of data pairs used to represent the loop. n therefore may be equal to the number of entries in the C-Q time series, however because hydrologic events usually vary in duration, we recommend resampling the data such that hysteresis samples and prototypes each share a consistent dimension. We expand on this more in section 3.

Alternative formats for samples and prototypes are also possible. For instance, Hamshaw et al. (2018) encoded loops as greyscale images with a resolution of 28×28 pixels for use in a classification algorithm. However, in our implementation, representing loops as sequences of (Q, C) pairs yielded better results through the SOM algorithm.

2.4 Quantifying similitude between loop~~s~~~~amples~~: The *distance function*

The distance function is a critical element of the SOM algorithm as it measures the similarity between a sample and each prototype. In the context of hysteresis, the distance function measures the similarity (or dissimilarity) between two hysteresis loops. This function directly affects the SOM algorithm's ability to extract the main patterns from the input data and arrange them in a coherent manner. Furthermore, this function is required during the *Analysis phase* (Fig. 3) to map new ~~samples~~hysteresis data to their associated loop prototype (BMU). While Euclidean distance is the default selection in most SOM applications, any function that computes the degree of similarity between two numeric arrays can be used such as Cosine similarity, Manhattan distance, Minkowski distance, etc. (Samarasinghe, 2016). Given our representation of hysteresis loops as sequences of Q-C data pairs, we propose using Dynamic Time Warping (DTW) to measure similarity between loops for application with SOM for hysteresis analysis.

DTW is an algorithm that measures the similarity between two time-series that may have slight timing mismatches. It has proven effective in clustering and classification across various domains involving sequential data (Ding et al., 2008; Dupas et al., 2015; Shokoohi-Yekta et al., 2017; Lee et al., 2020). Its primary advantage lies in its ability to prioritize the overall shape of the temporal sequences over a strict match of individual data points comprising the sequence. This is achieved by non-linearly stretching or compressing the time axis of one sequence to achieve optimal alignment with another, prior to computing the Euclidean distance between the aligned sequences. The resulting DTW distance reflects this alignment: it is upper bounded by the Euclidean distance when no alignment is possible, but yields a lower value when warping improves the match, indicating greater shape similarity. A comparison between Euclidean and DTW distances is presented in the Supplementary Information (section S1).

2.5~~2~~ ~~The training process~~SOM training and evaluation

2.5.1 SOM training and hyperparameter optimization

Map initialization

The SOM training algorithm ~~for training an SOM~~ for hysteresis analysis is illustrated in Fig 4.

First, training hyperparameters must be set. This includes the ~~Training an SOM begins with defining the~~ number of nodes to be included in the map lattice, which thereby determines the number of prototypes— (and, therefore, the number of distinct

Formatted: Space Before: 0 pt, Line spacing: Multiple 1.15 li
Formatted: Line spacing: Multiple 1.15 li
Formatted: Font: Italic
Formatted: Not Highlight
Formatted: Not Highlight
Formatted: Not Highlight
Formatted: Not Highlight
Formatted: Space After: 0 pt, Line spacing: Multiple 1.15
Formatted: Heading 2, Line spacing: Multiple 1.15 li
Formatted: Font: Bold, Italic
Formatted: Font: Italic
Formatted: Normal
Formatted: Normal, Space After: 12 pt, Line spacing: Multiple 1.15 li

loop types) — ~~used to describe the input data~~to be included in the trained map. While a larger map can represent a dataset with higher accuracy, they are often more difficult to visualize and interpret. Additionally, larger maps may produce prototypes that represent too few or none of the input samples, making the results more susceptible to noise and outliers. Ultimately, defining the map size relies on heuristic rules, domain intuition, and visual examination of the dataset (Vesanto, 2000; Kohonen, 2013). Importantly, however, the optimal size of the map should be refined iteratively, expanding the number of nodes until increases no longer result in meaningful improvements in the quality of the map (Céréghino and Park, 2009). We discuss metrics to assess the map quality in Section 2.~~5.2~~3.

Additional hyperparameters include the initial and final learning rate (α_0, α_f) and neighborhood radius (σ_0, σ_f). As explained below, they control ~~how much~~ the degree to which the map prototypes are adjusted during each step of the training process. ~~Finally, the~~The final hyperparameter ~~includes the~~training ~~, called~~is the number of epochs~~;~~, defined as the —training iterations~~s~~ where the entire dataset is processed once, — ~~which s~~defining ~~-~~which controls the length of the training process.

Once the map size is defined, initial prototypes must be assigned to each node. Random initialization using samples from the training dataset is commonly used, although more elaborate initialization approaches can also be employed (Attik et al., 2005). In the context of hysteresis, this means that a random set of hysteresis loops from the training dataset would be used to initialize the prototypes ~~included in each node, and those would be~~ which are then refined ~~over the course of map~~ throughout the training process.

Training loop

With this initial, untrained map, the training process is conducted by sequentially feeding random samples ~~(i.e., a C-Q hysteresis loop that is randomly selected from the training dataset) sequentially to the map~~ and adjusting the ~~untrained~~ prototypes to better match the input data ~~as follows~~. ~~First, f~~For each sample ~~(i.e.,: hysteresis loop)~~ $\boldsymbol{X}$, the ~~best matching unit (~~BMU~~)~~ is identified. ~~The BMU is~~ as the node ~~*j*~~ whose prototype ~~is closest~~ exhibits the highest similarity to the input sample as measured by ~~an appropriate distance function~~the DTW function ~~(e.g., Euclidean, cosine, Dynamic Time Warping, etc.)~~. Once the BMU is identified, the ~~2.4 Quantifying similitude between samples: The distance function~~

~~*The distance function*, used to identify the BMU, measures the similarity between two samples. This function directly affects the algorithm's ability to extract the main patterns from the input data and arrange them in a coherent manner. While Euclidean distance is the default selection in most SOM applications, any function that computes the degree of similarity between two samples can be used such as Cosine similarity, Manhattan distance, Minkowski distance, etc. (Samarasinghe, 2016).~~

~~Given that a hysteresis loop can be represented as a sequence of (Q, C) data pairs, an appropriate distance function for training an SOM of hysteresis loops is Dynamic Time Warping (DTW). DTW has demonstrated success in clustering and classification across various domains when working with time series data (Ding et al., 2008). Its primary advantage lies in its ability to prioritize the overall shape of the temporal sequences over a strict match of individual data points. This is achieved by dynamically stretching and compressing the time axis to obtain the highest possible alignment between sequences. The Euclidean distance between these aligned sequences is the final DTW distance measure. Hence, DTW distance is upper bounded by the Euclidean distance when no alignment between sequences is possible, but it yields a lower distance when some stretching or compression of the sequences result in a better match, indicating similar shapes. More details on the DTW algorithm and its application in water resources can be found in Lee et al. (2020) or Dupas et al. (2015) and some specifics on its use with two-dimensional time series data can be seen in Shokoohi-Yekta et al. (2017).~~

Formatted: Not Highlight

Formatted: Font: Italic

Formatted: Font: Bold, Italic

Formatted: Font: Italic

Formatted: Space After: 12 pt, Line spacing: Multiple 1.15 li

Formatted: Line spacing: Multiple 1.15 li

~~Since our objective is to capture similarities between loop shapes regardless of a strict match of individual (Q, C) data points, we consider DTW a suitable candidate for training SOMs for C-Q hysteresis loops. However, additional research is encouraged to better understand how different distance measures influence the trained map and devise tailored distance measures for this specific type of data.~~

learning parameters for the current iteration—learning rate (α) and neighborhood radius (σ)—are computed using a decay function. This decay function gradually reduces α and σ. ~~This produces a transition during the training from an initial ordering and placement phase where prototypes are adjusted to broadly represent the spatial organization of input data, to a fine-tuning phase where prototypes are refined to better represent the input samples (Samarasinghe, 2016).~~

resulting in a transition during training from an initial ordering and placement phase where prototypes broadly align with the spatial structure of the input data, to a fine-tuning phase where prototypes are refined to better represent the input samples (Samarasinghe, 2016).

Common choices of decay functions include hyperbolic, exponential, and linear (Kohonen, 2013). In our implementation, we adopted an exponential decay rate which varies from initial to final values defined during the map initialization (Fig. 4.).

In the next step of the training loop, neighborhood values (h_{BMU,η_k}) are computed. These values control the extent to which the prototype of each node η_k is updated during the current iteration based on the Euclidean distance—in map coordinates—between η_k and the BMU. This function plays a critical role in enabling SOM to produce smooth transitions across neighboring prototypes (i.e., ensuring that similar hysteresis loops are placed near one another). The neighborhood value reaches its maximum at the BMU and decreases with increasing distance from it, with the rate of decay being controlled by σ. In our implementation, we used the Gaussian kernel (Fig. 4), which is ~~T~~the most commonly used ~~-~~neighborhood function in SOM applications ~~is the Gaussian Kernel~~ (Kalteh et al., 2008).

Finally, the prototype m^{η_k} of each node η_k is updated using the learning rule (Eq. 1), which adjusts the prototypes toward the input sample. In ~~other words~~the context of hysteresis, each prototype ~~hysteresis~~ loop is iteratively refined to resemble C-Q hysteresis loops in the training data. This learning rule ensures that both the BMU and its neighboring nodes are moved closer to the current sample, allowing nearby prototypes to become more similar, which preserves the continuity of patterns across the map~~Next, the prototypes m^i of each node i are adjusted Eq. s~~to bring them closer to the input sample using equation (1).~~In other words, each prototype hysteresis loop is iteratively refined to resemble C-Q hysteresis loops associated with its surrounding region the map, meaning that neighboring prototypes become more similar to the input hysteresis loops and preserve the continuity of patterns across the map.~~ ~~with t~~The magnitude of adjustment ~~decreasing~~ decreases over time and with distance from the BMU, as determined by the decay and neighborhood functions. ~~The magnitude of the adjustment for each node is controlled by the learning rate (α) and the *neighborhood function* or smoothing kernel ($h^{i,j}$) centered at node j (the BMU for X). The most common neighborhood function is the Gaussian Kernel (Kalteh et al., 2008):~~

$$m^{\eta_k} \leftarrow m^{\eta_k} + \alpha \cdot h_{BMU,\eta_k} \cdot (\boldsymbol{X} - \boldsymbol{m}^{\eta_k}) \quad (1)$$

~~$$m_{t+1}^i = m_t^i + \alpha_t h_t^{i,j}(X - m_t^i) \quad (1)$$~~

Formatted: Space After: 12 pt, Line spacing: Multiple 1.15 li

Formatted: Highlight

Formatted: Not Highlight

Formatted: Right, Space After: 12 pt, Line spacing: Multiple 1.15 li

Formatted: Space After: 12 pt, Line spacing: Multiple 1.15 li

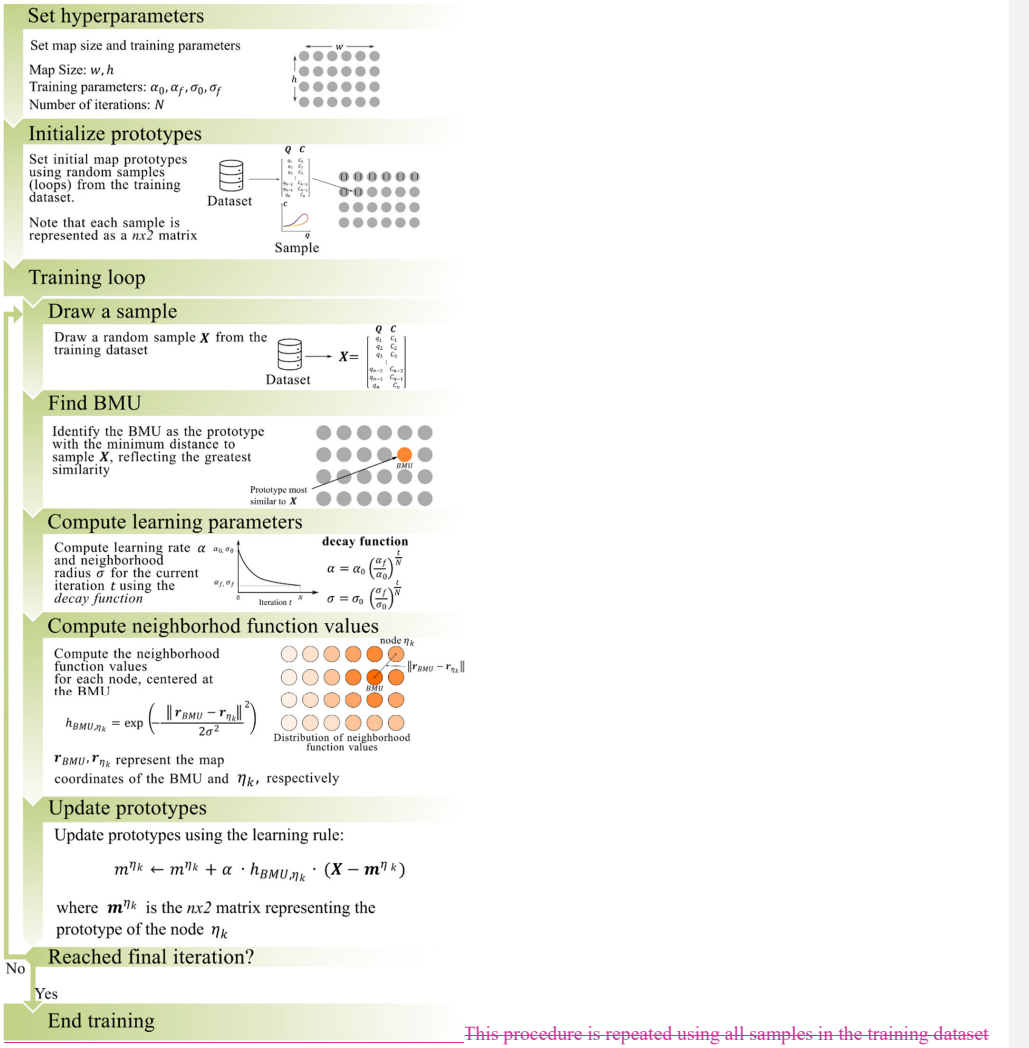

~~This procedure is repeated using all samples in the training dataset until the map stabilizes. During the training process, both the learning rate and radius of influence of the BMU (i.e., the spread of the smoothing kernel) are adjusted using a *decay function*, ensuring their values decrease over time (t). This produces a transition during the training from an initial ordering and placement phase where prototypes are adjusted to~~

~~broadly represent the spatial organization of input data, to a fine-tuning phase where prototypes are refined to better represent the input samples (Samarasinghe, 2016).~~

Figure 4. Workflow for training an SOM. α: learning rate, σ: neighborhood radius, subscripts 0, f indicate initial (first iteration) and final (last iteration) values, respectively. Q: Discharge, C: Concentration, n: length of the sequence of (Q, C) data pairs representing a loop (section 2.3). Other symbols are defined in the figure.

2.5.2~~3~~ Hyperparameter optimization ~~Quality assessment~~

Training hyperparameters—such as map size, learning rate, and neighborhood radius—directly influences the SOM's ability to preserve data topology and accurately represent input samples. To guide hyperparameter selection, we rely on two widely used SOM quality metrics: topographic error and quantization error. These metrics provide complementary insights into the structural fidelity and representational accuracy of the trained map.

Topographic error quantifies ~~the degree of topological preservation, i.e., how well~~the degree to which the SOM preserves the topological structure of the input space, that is, how well it maintains neighborhood relationships between loop types. A low topographic error indicates that similar loop prototypes are positioned close together, while dissimilar ones are placed farther apart. In the context of hysteresis, this means that loops with similar ~~shapes~~ amplitude, rotational direction and shape ~~and directions~~ should be placed close together. This metric is defined as the fraction of samples for which the Best Matching Unit (BMU) and the second BMU (i.e., the prototype with the second smallest distance to the input vector) are not adjacent on the map

~~Quality measures of Kohonen maps generally assess two map features: *topological preservation* and *quantization accuracy*. Topological preservation ensures that the map maintains the neighborhood relationships of the input space. Hence, a good topological preservation indicates that similar prototypes are placed close to each other and dissimilar prototypes are placed farther apart. Topological preservation can be quantified using the *topographic error*. This error is defined as the fraction of samples whose BMU and second BMU (i.e., the prototype with the second smallest distance to the input vector) are not neighbors~~ (Kiviluoto, 1996; Pölzlbauer, 2004). ~~Lower topographic errors indicate better topological preservation.~~ Lower values are preferred.

Quantization error, on the other hand, measures how closely the hysteresis prototypes ~~–~~approximate the input hysteresis samples. It is defined here as the average DTW distance between each sample and its BMU ~~On the other hand, quantization accuracy measures how well the prototypes approximate the input samples and is determined using the *quantization error*. This is defined as the average distance between each sample and its BMU~~ (Pölzlbauer, 2004). Lower quantization errors indicate ~~better~~ improved ~~representational~~ accuracy.

These two metrics often represent competing objectives~~. for example R~~as reducing one ~~one~~ metric may increase the other. Therefore, a balance must be achieved by evaluating SOMs trained under varying hyperparameter configurations. ~~For example~~These configurations should simultaneously consider:

Formatted: Heading 3

Formatted: Normal, Space After: 12 pt, Line spacing: Multiple 1.15 li

Formatted: Line spacing: Multiple 1.15 li

Formatted: Space After: 12 pt, Line spacing: Multiple 1.15 li

- Map size: Increasing the number of nodes generally reduces quantization error, as more prototypes can better approximate the dataset. However, larger maps may complicate visualization and interpretation. In the context of hysteresis analysis, the map size determines the number of distinct loop types ~~(i.e.: hysteresis loop prototypes)~~ to be included in the trained map.

~~Neighborhood radius: A wider radius promotes smoother transitions between hysteresis prototypes, reducing topographic error but potentially increasing quantization error. Conversely, a narrower radius sharpens prototype specialization, improving quantization accuracy error such that hysteresis loops are mapped to their prototypes relatively well, but risking *topological*~~

- ~~*fragmentation*~~, which can result in dissimilar hysteresis loops being placed close together.~~.~~
- Learning rate: This ~~I~~influences the speed and stability of convergence, with its decay profile affecting both error metrics.

~~A lower quantization error indicates that the prototypes closely resemble the input data. The quantization error can be calculated as a general measure for the map, taking the average over all samples, or as a distributed value over the map, where averages are calculated over the samples associated with each prototype. The latter offers a more detailed examination of the map quality across prototypes.~~

~~The topological error and the quantization error are competing objectives, as decreasing one generally increases the other. Therefore, a balance between both errors must be defined by assessing maps trained with varying hyperparameters such as the number of nodes (map size), the neighborhood spread, and the learning rate. Increasing the number of nodes results in lower quantization error because a larger number of prototypes can better approximate any given data set. Yet, this comes at the expense of more complex visualization and interpretation. The neighborhood spread has a large influence on both errors: higher spreads increase the radius of influence of each input sample over the map, producing smoother transition between prototypes. This reduces the topographic error but increases the quantization error. Conversely, a narrow neighborhood function isolates each prototype from its neighbors, allowing it to better match its associated samples. This, however, leads to less gradual transitions between prototypes and larger topographic errors. In broader applications, a trial-and-error approach is often followed where the user must choose the map that better suits their specific dataset (Clark et al., 2020).~~

In addition to quantitative metrics such as topographic and quantization errors, SOMs trained on hysteresis loops can be evaluated qualitatively ~~A Kohonen map of hysteresis loops can also be evaluated qualitatively since~~ as the prototype distribution can be easily visualized. The spatial distribution of prototypes offers a visual indication of topological preservation, with smooth and coherent transitions between loop types serving as a desirable trait.~~This is especially useful to assess the map's topological preservation which is reflected in a smooth and coherent transition between loop types. Hence, a suitable workflow for map selection could combine an initial assessment based on quantization and topographic errors, from which an initial subset of candidate maps could be selected. These candidates can then be visually inspected to select the optimum map for further analysis. This workflow is described in more detail in Section 2.5.~~

To fine-tune training hyperparameters, we propose the workflow illustrated in Fig. 5. First, multiple SOMs are trained across a grid of map sizes, learning rates, and neighborhood radii. The optimal map size is identified by examining the relationship between quantization error and number of nodes. While a decreasing trend in quantization error is expected as the number of nodes increases, the elbow method (Nainggolan et al., 2019) helps pinpoint the ~~point of diminishing returns~~optimal number of nodes for a map. Once the optimal size is selected, a subset of high-quality maps—trained with varying learning rates and neighborhood spreads—is extracted for closer inspection. These maps are chosen from the Pareto frontier (Koppa et al., 2019) of topographic and quantization errors~~(Koppa et al., 2019).~~

Formatted: Font: Italic

Formatted: Font: Italic

Formatted: List Paragraph, Space After: 12 pt, Line spacing: Multiple 1.15 li, Bulleted + Level: 1 + Aligned at: 0.25" + Indent at: 0.5"

Formatted: List Paragraph, Line spacing: Multiple 1.15 li, Bulleted + Level: 1 + Aligned at: 0.25" + Indent at: 0.5"

Formatted: List Paragraph, Line spacing: Multiple 1.15 li

Visual assessment of these ~~candidate~~ maps is then performed, guided by conceptual understanding of loop type similarities. In this application, ~~W~~we ~~prioritized~~ prioritized maps that exhibited~~ed~~ smooth transitions between similar loop types and clear separations between contrasting ones. Finally, ~~in our proof-of-concept,~~ we recommend further retraining the selected SOM to further improve~~d~~ map quality. While the initial selection from the Pareto frontier emphasized topological arrangement, retraining enhance~~s~~d quantization accuracy, yielding final error metrics that surpass~~ed~~ the original Pareto frontier.

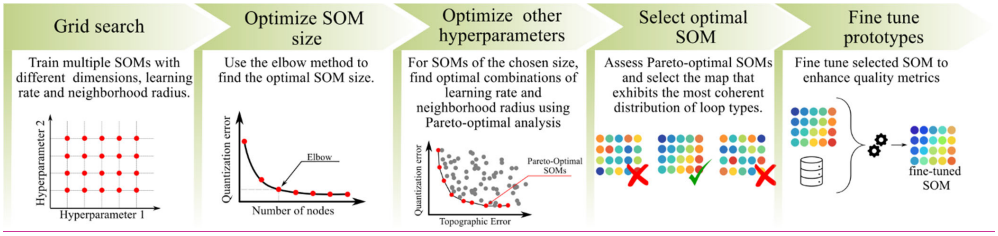

Figure 5. Workflow for fine-tuning SOM hyperparameters using a combination of quantitative metrics and qualitative assessment. The process begins with training multiple SOMs across a grid of map sizes, learning rates, and neighborhood radii. Quantization error is evaluated to identify the optimal map size using the elbow method. A subset of high-quality maps—selected from the Pareto frontier of topographic and quantization errors—is then examined in detail. SOM selection is based on visual inspection, prioritizing maps that exhibit coherent transitions between similar loop types and clear separation between contrasting ones. Finally, retraining of the selected SOM may enhance quantization accuracy.

2.6 Evaluation of a trained SOM for hysteresis analysis

The final step of the training phase (see Fig. 3) involves evaluating the SOM's ability to represent the full spectrum of loop types included in the curated dataset. We propose visual inspection as the most suitable approach, as it allows researchers to assess whether the distribution of prototypes reflects the diversity of loop shapes in the curated dataset and whether their arrangement aligns with conceptual expectations of loop similarities~~y~~ and differences. For instance, in our proof of concept, we examined whether loops from closely related classes (e.g., async-peak and sync-peak; see Fig. 6) were mapped to neighboring prototypes—indicating the SOM's ability to recognize shared geometric traits.

This evaluation helps identify which loop features are effectively captured by the SOM and which may require more nuanced analysis. Crucially, because SOM training is fully unsupervised, it does not rely on manual labels; instead, it organizes loops based solely on shape similarity, as defined by the DTW distance function.

Although quantitative metrics such as confusion matrices could be used to assess classification performance, we ~~chose~~recommend not to apply them here. Such metrics would require converting the SOM output into discrete categories, undermining its key advantage: preserving smooth transitions and continuous variation between loop types. ~~2.4 Quantifying similitude between samples: The *distance function*~~

~~The distance function, used to identify the BMU, measures the similarity between two samples. This function directly affects the algorithm's ability to extract the main patterns from the input data and arrange them in a coherent manner. While Euclidean~~

Formatted: Heading 2, Space After: 0 pt

Formatted: Space After: 12 pt, Line spacing: Multiple 1.15 li

Formatted: Normal, Space After: 12 pt

Formatted: Font: Not Italic

Formatted: Normal, Line spacing: Multiple 1.15 li

Formatted: Space After: 0 pt, Line spacing: Multiple 1.15 li

distance is the default selection in most SOM applications, any function that computes the degree of similarity between two samples can be used such as Cosine similarity, Manhattan distance, Minkowski distance, etc. (Samarasinghe, 2016).

Given that a hysteresis loop can be represented as a sequence of (Q, C) data pairs, an appropriate distance function for training an SOM of hysteresis loops is Dynamic Time Warping (DTW). DTW has demonstrated success in clustering and classification across various domains when working with time series data (Ding et al., 2008). Its primary advantage lies in its ability to prioritize the overall shape of the temporal sequences over a strict match of individual data points. This is achieved by dynamically stretching and compressing the time axis to obtain the highest possible alignment between sequences. The Euclidean distance between these aligned sequences is the final DTW distance measure. Hence, DTW distance is upper bounded by the Euclidean distance when no alignment between sequences is possible, but it yields a lower distance when some stretching or compression of the sequences result in a better match, indicating similar shapes. More details on the DTW algorithm and its application in water resources can be found in Lee et al. (2020) or Dupas et al. (2015) and some specifics on its use with two-dimensional time series data can be seen in Shokoohi-Yekta et al. (2017).

Since our objective is to capture similarities between loop shapes regardless of a strict match of individual (Q, C) data points, we consider DTW a suitable candidate for training SOMs for C-Q hysteresis loops. However, additional research is encouraged to better understand how different distance measures influence the trained map and devise tailored distance measures for this specific type of data.

2.5 Workflow for applying SOM in hysteresis analysis

A general workflow for utilizing the SOM algorithm for C-Q hysteresis analysis consists of two phases, as illustrated in Fig. 3. The first phase involves training an SOM to represent the spectrum of loop types for a particular dissolved or particulate constituent. To ensure the trained SOM adequately captures all primary loop types for a constituent, we recommend curating a dataset containing samples of all known loop types for the constituent under analysis during the training phase. Additionally – and critical for the objectives of this technical note – curating the training dataset facilitates evaluation of the algorithm's ability to represent and distinguish hysteresis loops. In practice, curating the training dataset also mitigates bias toward more frequently occurring loop types in natural systems by incorporating a balanced number of samples for each type. We discuss some advantages and limitations of this approach more in Section 5. During the training process, an SOM should be selected that provides a coherent arrangement and smooth transition between loop types (i.e., low topographic error) while accurately representing the training data (i.e., low quantization error).

The second phase of the workflow consists of using the trained SOM to characterize loop types from any dataset (assuming that they are of the same constituent of interest) to aid with analyzing hysteresis patterns in watersheds. This involves mapping each hysteresis loop in the dataset to its corresponding BMU within the trained SOM. Importantly, this procedure does not require reapplying the SOM algorithm itself; rather, it only requires the distance function to map each sample to its corresponding prototype. As demonstrated in our proof-of-concept in section 3, this approach can be employed to characterize the frequency distributions of loop types and explore associations between loop types and hydrological variables, thereby providing valuable insights into the underlying controlling mechanisms.

Formatted: Line spacing: Multiple 1.15 li

Formatted: Space Before: 0 pt, Line spacing: Multiple 1.15 li

Formatted: Space After: 0 pt, Line spacing: Multiple 1.15

Formatted: Line spacing: Multiple 1.15 li

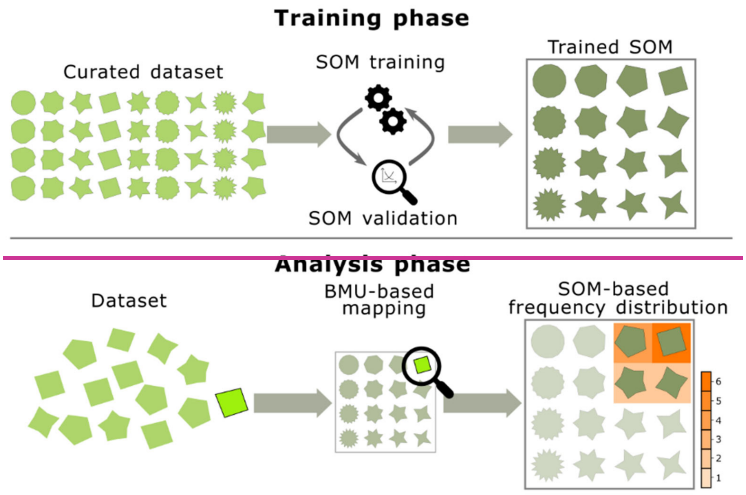

~~Figure 3. Workflow to generate an SOM for C-Q hysteresis loops (training phase) and apply the SOM for C-Q hysteresis analyses in watersheds (analysis phase). Here, we illustrate the generation of the SOM using different shapes, which are analogous to the hysteresis loop types that might be found for a dissolved or particulate constituent in a watershed. In the bottom panel (analysis phase), we demonstrate how hysteresis loops from a new dataset get mapped to the trained SOM, where the shade of orange represents the frequency with which the shape occurs in the dataset.~~

3 Applying SOM to turbidity-discharge hysteresis loops

We employ turbidity-discharge (T-Q) data ~~as~~ to develop a ~~proof~~proof-~~-~~of-~~-~~concept ~~to~~ and demonstrate the proposed workflow for training and applying SOM ~~in~~ for C-Q hysteresis analysis described in Section 2 and Fig. 3. The output of the training phase for the proof-of-concept is what we refer to as the *General T-Q SOM*. ~~Although sediment is the central focus of the current study,~~W ~~w~~e stress, however, that this workflow is adaptable to other constituents such as nutrients, dissolved solids, metals, and more. ~~We encourage f~~Future studies are encouraged to ~~expand on this approach to~~ explore its application across a broader range of constituents. ~~The following sections detail~~ exemplify ~~the implementation of this workflow (as shown in Fig. 3).~~

3.1 Training phase

3.1.1 Data curation and preprocessing

We surveyed the sediment transport literature to compile the primary loop types included in the curated dataset (Fig. ~~4~~6). Our review indicates that the majority of sediment hysteresis loop types recognized in the literature were originally identified by Williams (1989), with the *Figure L* loop introduced by Hamshaw et al. (2018). Additional studies have introduced nuanced variations of these loop types; for example, Bettel et al. (2025) introduced the "J" loop for a karstic system in Kentucky, USA which resembles concave-up loops. However, our analysis suggests that sediment hysteresis loop diversity can largely be

Formatted: Space After: 0 pt
Formatted: Space Before: 0 pt
Formatted: Line spacing: Multiple 1.15 li
Formatted: Space Before: 0 pt, Line spacing: Multiple 1.15 li
Formatted: Not Highlight
Formatted: Line spacing: Multiple 1.15 li

explained by the 17 loop types identified in Fig. 64, encompassing *single-line* (first row in Fig. 6), ~~*Figure 8,*~~ *clockwise* (second row in Fig. 6), and *counterclockwise* (third row in Fig. 6) topologies. ~~Complex~~ Irregular loops (e.g., complex loops) were excluded ~~from the curated dataset~~ due to their ~~irregularity~~abnormality and lack of a standardized classification system. While additional loop types may exist beyond those included, they are generally infrequent and relevant only to specific studies or watersheds. Therefore, since our training dataset incorporates most of the known sediment hysteresis loop types, we refer to the output of the training phase as the *General T-Q SOM*. We discuss the incorporation of less common loops in Section 5 and encourage the development of tailored SOMs to accommodate specialized applications.

The curated dataset consists of 20 samples for each loop type, resulting in a total of 340 loops. Loops were manually delineated using publicly available discharge and turbidity data collected at 15-minute intervals by the USGS across 37 stream gauges in the United States. Data were retrieved from the National Water Information System using the Data Retrieval Python package (Hodson et al., 2023). Event delineation was supported by a custom-built application designed to label hydrologic time series.

Watershed selection and event delineation followed the criteria outlined below:

- Only rainfall-dominated hydrologic events were included; heavily regulated rivers and snowmelt-dominated watersheds were excluded.
- Multi-peak events were split into single-peak events if turbidity receded fully before the onset of the subsequent peak.
- Irregular loops (such as complex loops) or loop shapes that did not conform to the typologies illustrated in Fig. 6 were excluded.
- We then manually classified the loop shape to one of the typologies illustrated in Fig. 6 according to visual comparison until an even number of event types was identified.

We should note that while manual classification during data curation can be somewhat subjective, this is a minor concern since the SOM is not constrained to enforce strict boundaries between loop types and does not see the assigned label~~sed~~. For example, whether a narrow clockwise loop is labeled as a *single line* or a *clockwise Sync-Peak* loop may be debatable—but including it in training allows the SOM to learn the gradual transition between these shapes, independent of the assigned label. Additionally, while dataset curation is a time-intensive task, requiring the extraction of multiple hydrologic events from several watersheds, it is typically performed only once for each constituent's SOM. Once trained, the SOM can be readily shared and reused by other researchers without the need for retraining.

The Supplementary Information provides detailed site information and data periods (Table S1~~1~~), while the complete set of loops included in the training dataset is presented in Fig~~s~~. S3~~1 and S2~~.

Formatted: List Paragraph, Line spacing: Multiple 1.15 li, Bulleted + Level: 1 + Aligned at: 0.25" + Indent at: 0.5"

Formatted: Line spacing: Multiple 1.15 li

Formatted: Font: Italic

Formatted: Font: Italic

Formatted: Font: Italic

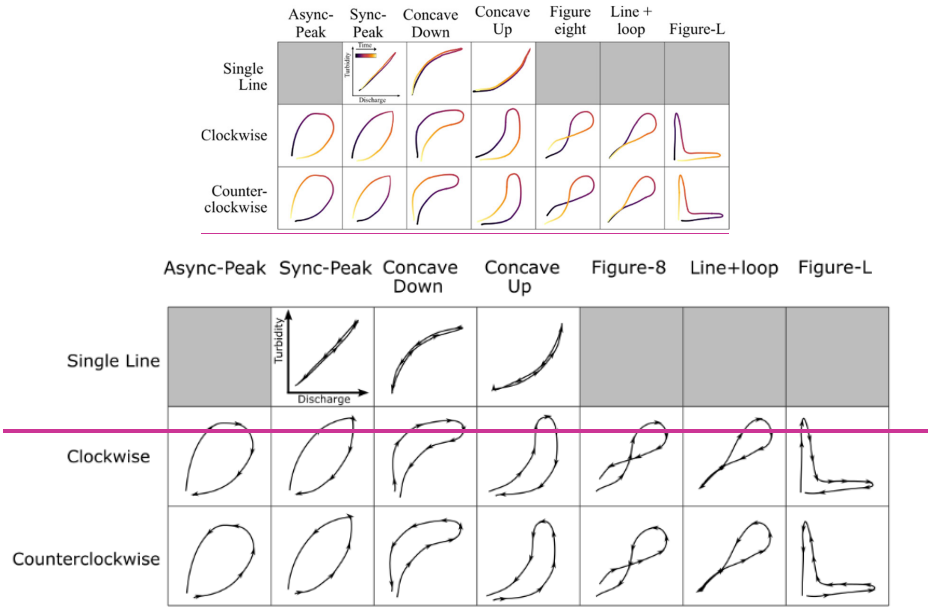

Figure 6~~4~~. Loop types considered in the training dataset. Except for Figure-L loops—introduced by Hamshaw et al. (2018)—all loop types were originally described by Williams (1989). While past studies often lump together all subclasses within the broader categories of Single Line, Clockwise, and Counterclockwise loops, our dataset introduces a more granular classification that captures multiple shape variations within each type, such as differences in concavity, which reflect the relative spread of the sedigraph with respect to the hydrograph, or Figure-L loops, which indicate~~s~~ strong decoupling between discharge and sediment concentration. Readers interested in the hydrological interpretation of these loop types are encouraged to consult the original studies.~~Loop types considered in the training dataset. All loop types, with the exception of *Figure-L* loops, were initially described by Williams (1989). *Figure-L* loops were introduced by Hamshaw et al. (2018)~~

The SOM algorithm requires samples to be represented as arrays with an equal number of elements. Given that loops in the dataset consist of variable-length sequences of ~~(Q, T)~~Q-T data pairs, we implemented a preprocessing procedure to convert all loops into sequences of equal length, ensuring compatibility with the SOM algorithm. This procedure is illustrated in Fig. 7~~5~~ and involves the following steps. First, we applied a moving median with a 5-point window to the turbidity values to reduce ~~the~~ random ~~influence of~~ noise ~~outliers~~ (Fig. 7~~5~~b). Second, the Q-T data were scaled to a [0,1] interval using min-max normalization based on the minimum and maximum values for each event. This scaling, commonly applied prior to the calculation of hysteresis indices, facilitates comparison between loops of different magnitudes (Lloyd et al., 2016); and third, we interpolated the resulting variable-length, scaled T-Q data (Fig. 7~~5~~c) to produce equal-length sequences (Fig. 7~~5~~d) of 100 data pairs. The interpolation ensures that data points are equally spaced in the Q-T plane.

Formatted: Justified

Formatted: Space After: 12 pt, Line spacing: Multiple 1.15 li

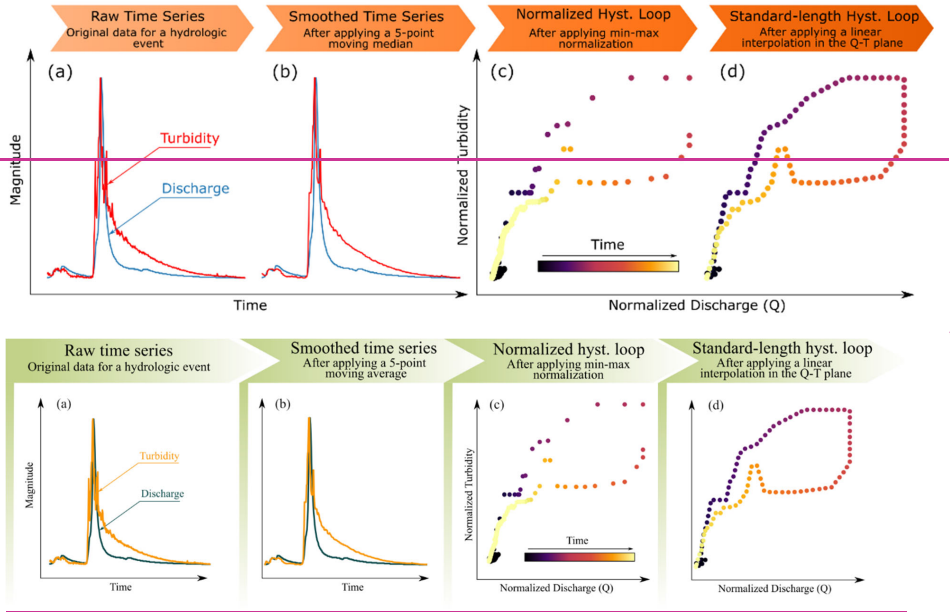

Figure ~~5~~7. Workflow illustrating data preprocessing steps: a) original discharge and turbidity data~~.~~, b) ~~A~~a 5-point moving median was applied to turbidity data to mitigate outliers~~,~~ c) Q-T data were min-max normalized to a [0,1] interval~~.~~, d) the scaled, variable-length data were interpolated into equal-length sequences of 100 data pairs.

3.1.2 SOM training and ~~validation~~hyperparameter optimization

SOM training and hyperparameter tuning followed the workflows explained in section 2.5. ~~The map training process involves three key steps: map size selection, map topology selection, and map refinement (Samarasinghe, 2016).~~

~~During the map size selection step,~~ SOM~~s~~ sizes ~~ranging~~ ranged from 5x5 to 13x13 nodes, with ~~were trained using a grid search approach, varying~~ initial ~~hyperparameters such as~~ neighborhood ~~spread~~ radii varying from ~~(~~0.5~~–~~ to 13~~)~~ and initial learning rate~~s~~ ~~(~~from 0.05~~–~~ to 0.9~~.) across five epochs~~ Final values for neighborhood radius and learning rate were set at 0.3 and 0.01, respectively. Training was conducted over five epochs, meaning the entire dataset was presented to the algorithm five times, resulting in 1700 iterations per ~~hyperparameter combination~~hyperparameter combination (340 samples × 5 epochs). ~~I~~; ~~resulting i~~n total, approximately 900 ~~trained maps~~SOMs were trained.

The training algorithm was implemented in Python, using the Numpy library (Harris et al., 2020) for array computations and the DTW implementation provided by the tslearn package (Tavenard et al., 2020). Training time per SOM ranged from 20 seconds for smaller maps (5×5 nodes) to 140 seconds for larger maps (13×13 nodes), with a total execution time of

Formatted: Space After: 12 pt, Line spacing: Multiple 1.15 li

Formatted: Line spacing: Multiple 1.15 li

approximately 15 hours on an AMD Ryzen 9 PRO 5945 12-Core Processor (3.00 GHz). It is important to note that this computing time applies only to the training phase. Once trained, the SOM can classify hundreds of loops in a fraction of a second using the DTW algorithm.~~. Highly distorted maps, identified by topographic error, were excluded. The elbow method was then applied to determine the optimal map size, where increasing the number of nodes no longer significantly reduced quantization error (Nainggolan et al., 2019).~~

Optimal SOM selection, as illustrated in the fourth step of Fig. 5, was guided by our conceptual understanding of sediment transport loop types. For instance, maps were ~~ranked higher~~prioritized when clockwise and counterclockwise *Figure L* loops were placed farther apart than clockwise and counterclockwise *Sync-Peak* loops (see Fig. 6), reflecting the greater temporal mismatch between discharge and turbidity in the former. This conceptual prioritization helped ensure that the SOM captured meaningful distinctions in loop behavior. ~~Once the optimal map size was identified, we evaluated a subset of maps to find the one that best captured and organized the spectrum of loop types in the dataset. This subset was chosen through Pareto-optimal analysis, identifying maps on the frontier of topographic and quantization errors. The general arrangement of loop types was assessed based on our conceptual understanding of similarities and differences between loop types to ensure smooth transitions between similar loop types and clear separations between contrasting ones. For example, maps were ranked higher when clockwise and counterclockwise *Figure L* loops were placed farther apart than clockwise and counterclockwise *Sync-Peak* loops (see Fig. 4), as the former loop shapes indicate more pronounced time mismatches between discharge and turbidity.~~

In the final refinement step, the selected SOM was retrained for an additional five epochs to enhance quantization accuracy. While the initial training emphasized the overall arrangement of loop types, this refinement focused on improving the alignment between each BMU and its associated samples. To achieve this, a constant neighborhood spread of 0.45 and learning rate of 0.05 were employed.

3.1.3 Evaluation

We followed the principles defined in section 2.6 to evaluate the trained SOM's ability to represent the full spectrum of loop types in the curated dataset. Specifically, we visually examined whether loops from the same or similar categories (e.g., *single-lines*) were consistently mapped to prototypes that reflect their characteristic shapes. We also assessed the extent to which the SOM distinguished~~s~~ between conceptually contrasting C–Q dynamics, such as clockwise versus counterclockwise ***Figure L*** loops, indicating its capacity to capture meaningful differences in loop behavior.~~In the final refinement step, the selected map underwent retraining for an additional five epochs. While the map from the preceding step focused on optimizing the overall arrangement of loop types, this step targeted enhanced quantization accuracy. To achieve this, the map was retrained using a reduced neighborhood spread, updating only the Best Matching Unit (BMU) during each iteration. This adjustment significantly improved the alignment between each BMU and its associated samples. A constant learning rate of 0.05, with no decay, was maintained throughout this refinement.~~

Formatted: Font: Italic
Formatted: Font: Italic
Formatted: Heading 3, Space After: 0 pt
Formatted: Line spacing: Multiple 1.15 li
Formatted: Font: Italic
Formatted: Font: Italic

~~3.1.3 Map quality evaluation~~

~~The final evaluation step aimed to assess the SOM's ability to represent the full spectrum of loop types included in the training dataset. Each loop was mapped to its corresponding prototype (i.e., BMU) and underwent a visual examination to assess how loops within a given class aligned with their prototypes. Specifically, we evaluated the consistency of loop types mapped to a given prototype, as well as the resemblance of individual loops to their BMU. Additionally, we evaluated the extent to which loops from the same or closely related classes (e.g., *async-peak* and *sync-peak;* see Fig. 4) were mapped to neighboring prototypes indicating the SOM's ability to recognize shared shape characteristics in alignment with conceptual classifications. This evaluation approach highlights the features that the SOM algorithm effectively captures while identifying those requiring more nuanced analysis. Since the SOM training process is fully unsupervised, it disregards manually assigned labels, relying solely on loop shape to detect similarities and differences. We note that while the curated dataset was manually labeled (to aid with training the model on a balanced dataset), these labels are not seen by the model. Finally, we chose to avoid quantitative classification metrics, such as confusion matrices, to evaluate the ability of the SOM to characterize hysteresis loops, as they would require converting the SOM mapping into a nominal classification scheme—undermining SOM's key advantage of preserving gradual transitions between loop types.~~

3.2 Analysis phase

~~Once trained and evaluated, To we~~We demonstrate the application of the trained and evaluated T-Q ~~trained~~ SOM (referred to henceforth as the *General T-Q SOM*) for analyzing hysteresis patterns~~, we~~ using a ~~collected a~~ secondary dataset, not used during training, consisting of T-Q hysteresis loops from three monitoring stations. These watersheds were selected to illustrate two primary analyses for characterizing hysteresis patterns: (1) exploring the frequency distribution of loop types within a watershed (gages 07364130 and 03254480), and (2) identifying associations between loop types and hydrologic variables (gage 03289000).

The coordinates of these stations and key properties of their associated watersheds are provided in Table 1. Watershed boundaries were obtained from the USGS StreamStats online application, watershed slope was calculated using the USGS 3DEP (10m) digital elevation model, urban area was extracted from the 2021 National Land Cover Database, and soil texture was extracted from the Probabilistic Remapping of SSURGO (POLARIS) database (Chaney et al., 2019).

~~Theseis dataset watersheds were selected to illustrate supports two primary analyses for characterizing hysteresis patterns: (1) exploring the frequency distribution of loop types within a watershed (gages 07364130 and 03254480), and (2) identifying associations between loop types and hydrologic variables (gage 03289000).~~

Table 1. USGS monitoring stations and watershed properties used in the SOM-based analysis phase.

USGS code	07364130	03254480	03289000
Latitude	33.96	38.84	38.04
Longitude	-91.69	-84.53	-84.63
Watershed Area (km^2)	311	47	62
Watershed Mean Slope (m/m)	0.012	0.13	0.08
Watershed Urban Area (%)	2.03	1.31	15.8
Mean Discharge ($m^3\ s^{-1}$)	7	0.85	1.2

Formatted: Space Before: 0 pt, Line spacing: Multiple 1.15 li

Formatted: Line spacing: Multiple 1.15 li

Formatted: Space After: 12 pt

Formatted: Line spacing: Multiple 1.15 li

Formatted: Line spacing: Multiple 1.15 li

Formatted: Line spacing: Multiple 1.15 li

Formatted: Line spacing: Multiple 1.15 li

Formatted: Line spacing: Multiple 1.15 li

Formatted: Line spacing: Multiple 1.15 li

Formatted: Line spacing: Multiple 1.15 li

Soil Texture	**Sand (%)**	9	6	6
	Silt (%)	50	61	64
	Clay (%)	41	33	30

Formatted: Line spacing: Multiple 1.15 li

Formatted: Line spacing: Multiple 1.15 li

Hydrologic events for watersheds 07364130, 03254480, and 03289000 were manually extracted from 15-minute discharge and turbidity data provided by the USGS and retrieved via the National Water Information System. For station 03289000, turbidity data were collected by the University of Kentucky using a YSI 6-series optical turbidity sensor. All loops underwent preprocessing consistent with the curated dataset (see Section 3.1.1). This process resulted in 27, 54, and 70 events for gages 07364130, 03254480, and 03289000, respectively. Additional hydrologic variables were included for watershed 03289000, including rainfall 15~~-~~hours prior to events, average discharge over the 5 preceding days, and the ratio of old-water to event-water, derived from our previous work in this watershed (Marin-Ramirez et al., 2024). These variables serve as proxies for rainfall, antecedent moisture conditions, and dominant hydrologic pathways associated with each event, respectively.

For each site, loop frequency distributions were generated by mapping individual hysteresis loops to their corresponding ~~SOM~~ BMU prototype~~s~~ and visualizing ~~them~~ the results as heatmaps atop the *General T-Q SOM*. ~~Distributions f~~For gages 07364130 and 03254480, we ~~were~~ compared these heatmaps to ~~to those obtained using the~~ frequency distributions of hysteresis index, as ~~-~~proposed by Zuecco et al. (2016).

For watershed 03289000, the ~~*trained SOM*~~ *General T-Q SOM* was employed to explore relationships between loop types and hydrologic variables. This ~~station~~ watershed was selected based on prior understanding of the hydrologic processes controlling sediment transport in the watershed (Marin-Ramirez et al., 2024), providing a framework for validation and comparison with the trained ~~*SOM*~~*General T-Q SOM*. Associations between hydrologic variables and loop types were ~~initially~~ qualitatively explored through visual analysis, where median values of the variables were plotted across SOM prototypes as heatmaps to reveal patterns linking high or low values with specific loop types.

To further ~~quantitatively assess~~quantify these associations, we applied a correlation-based approach ~~was applied~~using multiple linear regression. The ~~First,~~ BMU coordinates of each loop ~~were transformed into a two-dimensional representing each loop type. This two-dimensional index~~ served as ~~the~~ predictor variable~~s~~ ~~in a multiple linear regression model.~~ and the response variable was a ~~R~~rank-normalized hydrologic ~~variables~~metric (precipitation, antecedent discharge, and the ratio of old-water to event-water) ~~were used as predictands~~~~response variables~~~~,~~. Rank-normalization ~~allowing~~ ~~allowed~~enabled the model to capture non-linear, monotonic relationships. However, non-normalized variables could also be employed. Correlation coefficients ~~were then used to evaluate~~quantified the strength of ~~each~~ association~~s~~~~s~~, while the regression~~-~~plane~~'s~~ coefficients ~~represented~~ indicated the direction of maximum change in the hydrologic variable across the ~~*SOM*~~*General T-Q SOM*.~~gradients showing the direction of maximum change in the hydrologic variable.~~ These gradients helped identify which loop types were associated with higher or lower values of the hydrologic variables. Results were visualized using a biplot chart, enabling simultaneous exploration of relationships between loop types and multiple hydrologic variables.

4 Results

4.1 ~~SOM t~~Training the *General T-Q SOM*

4.1.1 Balancing quantization and topographic errors

The elbow method identified 8×8 nodes as the optimal map size for the *General T-Q SOM*, where quantization ~~accuracy~~ error stabilizes (Fig. ~~8~~6a). While larger maps may achieve lower quantization errors, this improvement comes at the cost of increased distortion, reflected by high topographic errors. Moreover, visual inspection of maps with varying sizes (not shown) revealed no advantages in terms of the number of loop patterns represented.

The pareto frontier of these 8×8 maps shows the expected inverse relationship between topographic and quantization errors (Fig. ~~8~~6b). After visually examining six maps along this frontier, the map with the best overall distribution of loop types was selected (black dot shown in Fig. ~~8~~6b~~, refer to section S3 in the Supplementary Information for an example of a discarded SOM~~). We favored maps with clear separations and smooth transitions between clockwise and counterclockwise loops and between concave-up and concave-down loops, which are representative of both the timing and duration of sediment transport during events (refer to section S3 in the Supplementary Information for an example of a discarded SOM). The selected map exhibited a low topographic error (0.006) but a relatively high quantization error (0.73). However, the quantization error was improved during the refinement phase. The final map achieves a well-balanced trade-off between topological preservation (TE = 0.04) and quantization ~~accuracy~~ error (QE = 0.66).

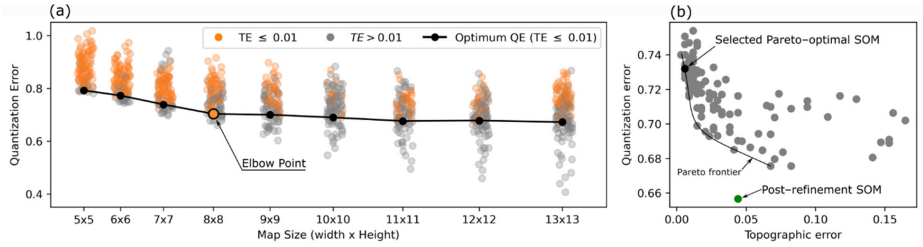

Figure ~~8~~6. a) Quantization Error (QE) across varying map sizes, illustrating the expected decrease in QE as map size increases. While larger maps continue to lower the minimum QE, this reduction stabilizes when considering maps with low Topographic Error (TE ≤ 0.01). Similar stabilization patterns are observed across other TE thresholds (0.05 and 0.1). b) Scatterplot displaying QE and TE for 8×8 maps. The map selected after visual inspection is highlighted, alongside the final QE and TE following map refinement training, which corresponds to the *General T-Q SOM*.

4.1.2 The General T-Q SOM: A trained SOM for sediment hysteresis analysis

Fig. ~~9~~7 shows the trained SOM generated using the curated T-Q dataset, which we refer to as the *General T-Q SOM*~~, which may be used for sediment hysteresis analysis~~. The map provides an organized representation of most loop types from the curated dataset, with smooth transitions between different classes. In general, the map arranges loop shapes based on the loop amplitude, rotational direction (clockwise or counterclockwise), and concavity following the directions defined by the diagonals. These diagonals can be conceptualized as axes of a Cartesian plane: the diagonal running from the lower left to the

Formatted: Space Before: 0 pt, Line spacing: Multiple 1.15 li

Formatted: Font: Italic

Formatted: Space After: 12 pt, Line spacing: Multiple 1.15 li

Formatted: Space Before: 0 pt, Line spacing: Multiple 1.15 li

Formatted: Space After: 12 pt, Line spacing: Multiple 1.15 li

upper right (LL-UR) represents variations in loop amplitude and rotational direction, while the diagonal from the upper left to the lower right (UL-LR) represents changes in concavity.

The LL-UR diagonal illustrates the expected progression between clockwise and counterclockwise loops as illustrated in Fig. 1. Wide clockwise and counterclockwise loops occupy the extreme ends of this diagonal, while single lines are positioned near the center of the transition. *Figure L* loops notably appear at opposite ends of this transition, emphasizing their role as extreme cases of clockwise and counterclockwise loops, as they represent a pronounced mismatch in concentration between the rising and falling limbs (Fig. 2). The UL-LR diagonal, on the other hand, captures the transition from concave-up to concave-down loops. Hence, all concave-up (*clockwise*, *counterclockwise* and *single lines*) loops are placed in the upper-left quadrant of the map, while concave-down (*clockwise*, *counterclockwise* and *single lines*) occupy the lower-right quadrant.

Furthermore, these diagonals effectively serve as symmetrical axes, highlighting the map's coherent and robust topological structure. For example, clockwise loops along the LL-UR diagonal (e.g., H1, G2, F3, E4) are mirrored by their counterclockwise equivalents (e.g., D5, C6, B7, A8).

Interestingly, the map also reveals the presence of loop types not explicitly considered during data curation. For instance, it distinguishes between concave-up and concave-down clockwise *line+loop* loops (e.g., prototypes C1 and H6), underscoring its ability to capture differences in concavity. On the other hand, *Figure-eight* ~~*8*~~ loops are less accurately represented—they appear as narrow loops placed close to single lines (e.g., D4, E5). This suggests that the map may have less discriminatory power for *Figure-eight* ~~*8*~~ loops.

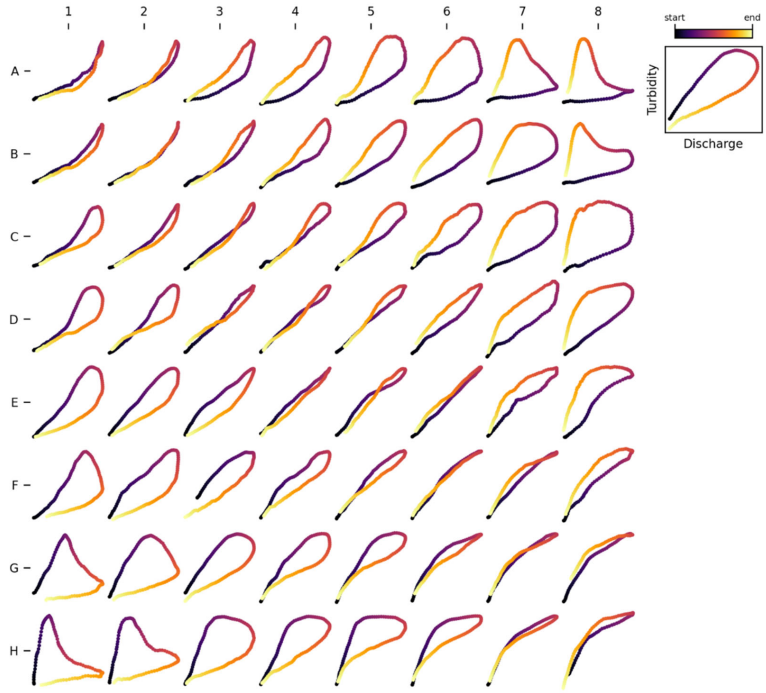

Figure ~~7~~9. ~~Kohonen map~~SOM for Turbidity – Discharge (T-Q) hysteresis analysis. The map was trained using a curated dataset comprising 17 different loop types, with 20 samples for each loop type. We refer to this as the *General T-Q ~~Map~~SOM*.

4.1.3 ~~Map E~~evaluation of the *General T-Q SOM*

To evaluate the efficacy of the trained SOM ~~*Kohonen map*~~ in discriminating between different loop types, we mapped each loop in our curated dataset to its corresponding prototype (i.e., its BMU). As shown in Fig. ~~8~~10, the results are consistent with our manual classifications, noting that the manual classification was not seen by the model as part of the training process. In particular, the map effectively distinguishes rotational direction (clockwise, counterclockwise), loop amplitude (ranging from wide loops to single lines), and concavity. However, the self-intersecting structure of *Figure-eight ~~8~~* loops is less effectively captured.

Single-line loops are consistently mapped to prototypes that best represent their shape along the UL-LR diagonal (Fig 10~~8~~a), while *Figure L* loops are properly mapped to their corresponding prototypes at the map's corners (Fig ~~8b~~10b, ~~8c~~10c). The

Formatted: Justified, Space After: 12 pt, Line spacing: Multiple 1.15 li

Formatted: Space After: 12 pt, Line spacing: Multiple 1.15 li

Formatted: Font: Italic

Formatted: Space Before: 0 pt, Line spacing: Multiple 1.15 li

Formatted: Space After: 12 pt, Line spacing: Multiple 1.15 li

spectrum of clockwise and counterclockwise loops (including *Async-Peak*, *Sync-Peak*, *concave-down*, *concave-up* and *line+loop* loops) is also well-represented, with clockwise loops occupying the lower-left quadrant and counterclockwise loops in the upper-left quadrant of the map (Fig ~~8b~~10b, ~~8c~~10c).

Overlap exists between some loop types, which is expected due to the similar topologies of many loops (see Fig. 1). For instance, several counterclockwise *Async-Peak* and *Sync-Peak* loops map to the same prototype (prototype B6, ~~(~~Fig. ~~8c~~10c), while their clockwise counterparts group under prototype E2 (Fig. ~~8b~~10b). A closer examination of these clusters (Fig. ~~9~~11) reveals that they comprise of loops sharing similar characteristics in terms of direction, amplitude, and concavity—or the lack thereof—demonstrating the algorithm's effectiveness in discriminating loops based on these features.

Figure ~~8~~ eight loops, in contrast, exhibit a more dispersed mapping, often associated with prototypes that lack a clear *Figure ~~8~~ eight* resemblance. Nonetheless, the mapping is not entirely flawed. Closer examination reveals that *Figure ~~8~~ eight* loops are matched to prototypes resembling their loop amplitude, direction, and concavity (see Fig. ~~9~~11). Note that in our manual classification, these *Figure eight ~~8~~* loops were categorized as clockwise based on the rotational direction of the second loop (i.e., the one with larger ~~C~~T-Q values). Nevertheless, they were mapped to counterclockwise loops following the rotational direction of the dominant loop, which in this case is the first loop. Despite this apparent contradiction, we consider this an acceptable representation of these loops.

Overall, we consider the ~~trained map~~ trained SOM to perform satisfactorily when representing and discriminating between a broad spectrum of loop patterns associated with sediment transport, as informed by our survey of the sediment transport literature~~.~~, therefore giving us confidence when ~~Hence, we will~~ referring to this ~~to this~~ trained SOM as the *General T-Q SOM*. Next, ~~As such, we refer to the trained map as the *General T-Q SOM*. W~~we ~~discuss some~~explore specific uses of the *General T-Q SOM* for broader hysteresis ~~analyses~~analysis ~~in Section 5~~.

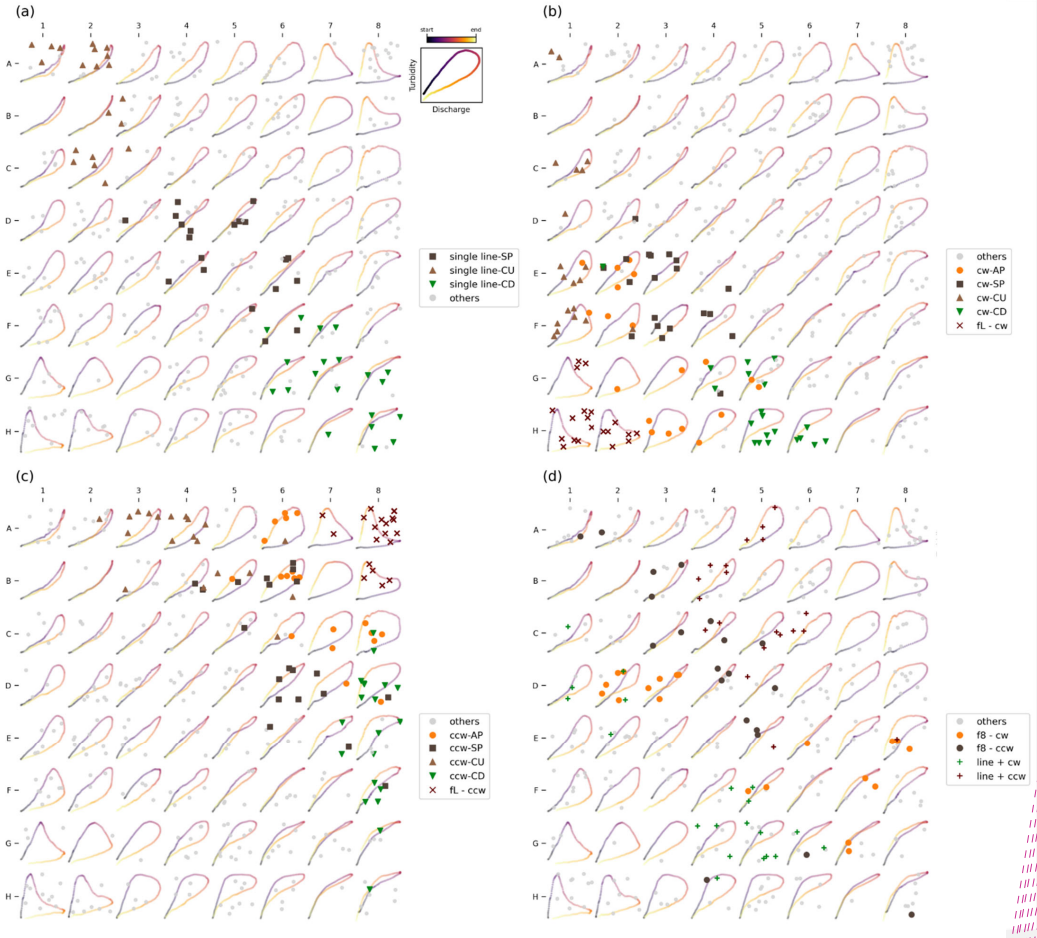

Figure 108. Mapping of all samples from the curated loop dataset to their respective BMUs on the trained SOM. For visual clarity, loop types and their mappings are organized into four distinct panels: (a) *single-line* loops; (b) *clockwise* loops including *Async*, *Sync*, *Concave*, and *Figure-L*; (c) *counterclockwise* loops including *Async*, *Sync*, *Concave*, and *Figure-L*; and (d) *Figure-eight* and *Line+loops*. Acronyms used in the figure include: SP – *Sync-Peak*, AP – *Async-Peak*, CU – *Concave-Up*.

Formatted: Font: Not Italic
Formatted: Font: Italic
Formatted: Font: Italic
Formatted: Font: Italic
Formatted: Font: Italic
Formatted: Font: Italic
Formatted: Font: Italic
Formatted: Font: Italic
Formatted: Font: Italic
Formatted: Font: Italic
Formatted: Font: Italic
Formatted: Font: Italic
Formatted: Font: Italic
Formatted: Font: Italic

CD – *Concave-Down*, ccw – *Counterclockwise*, cw – *Clockwise*, *fL – Figure-L*, f8 – *Figure-eight*.~~The figure shows the mapping of all samples from each loop type (see Fig. 3) in the curated dataset to their respective Best Matching Unit (BMU) on the Kohonen map. To enhance clarity, loop types and their corresponding mappings are divided into four distinct groups. SP: *Sync-Peak*, AP: *Async-Peak*, CU: *Concave-Up*, CD: *Concave-Down*, ccw: *Counterclockwise*, cw: *Clockwise*, fL: *Figure-L*, f8: *Figure 8*~~

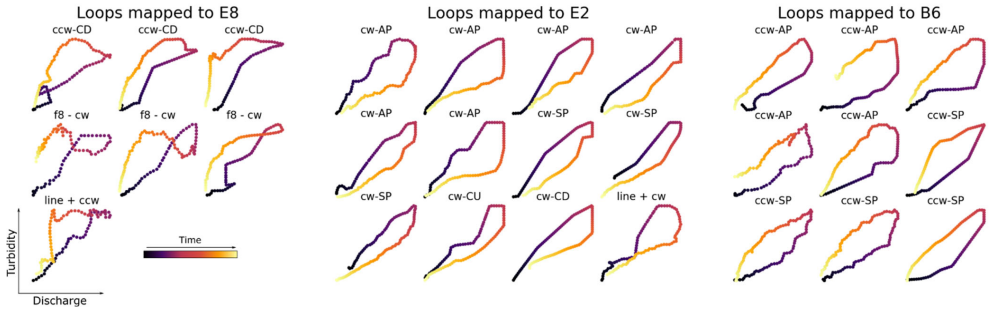

Figure 11~~9~~. Loops mapped to prototypes E8, E2 and B6 along with their respective classes as defined in the manual classification. While loops from different classes in the curated dataset are mapped to the same prototype, this figure underscores their similarities in terms of loop direction, amplitude, and concavity—or the lack thereof. This highlights the inherently fuzzy boundaries that exist between certain loop types. SP: *Sync-Peak*, AP: *Async-Peak*, CU: *Concave-Up*, CD: *Concave-Down*, ccw: *Counterclockwise*, cw: *Clockwise*, fL: *Figure-L*, f8: *Figure-eight ~~8~~*

4.2 Analysis of hysteresis loops using the *General T-Q SOM*

4.2.1 Characterizing frequency distributions of hysteresis loop types

Fig. 10~~2~~a shows the frequency distributions of hysteresis loop types found in watersheds 03254480 and 07364130 as heatmaps over the *General T-Q SOM,* contrasted with Fig. 12~~0~~c, which shows the distributions of hysteresis index. While both watersheds predominantly exhibit clockwise loops, the *General T-Q SOM* reveals additional insights that the hysteresis index distribution cannot capture. ~~Namely~~Specifically, watershed 03254480 shows more concave-down loops, while watershed 07364130 primarily shows concave-up loops. ~~Importantly, t~~These differences are overlooked by the hysteresis index, as its frequency distributions are statistically indistinguishable (two-sided Smirnov-Kolmogorov test, $p = 0.997$).

Fig. 13~~1~~ reinforces this by illustrating the distribution of hysteresis index values across the map's prototypes, confirming that the hysteresis index does not account for loop concavity. For instance, prototypes along the diagonal from E1 to H4 exhibit

Formatted: Font: Italic
Formatted: Font: Italic
Formatted: Font: Italic
Formatted: Font: Italic
Formatted: Font: Italic
Formatted: Font: Italic
Formatted: Space Before: 0 pt
Formatted: Space After: 12 pt, Line spacing: Multiple 1.15 li

identical hysteresis index values, despite a noticeable transition from concave-up to concave-down loops. This highlights the *General T-Q SOM's* ability to capture subtle variations in loop characteristics that the hysteresis index fails to detect.

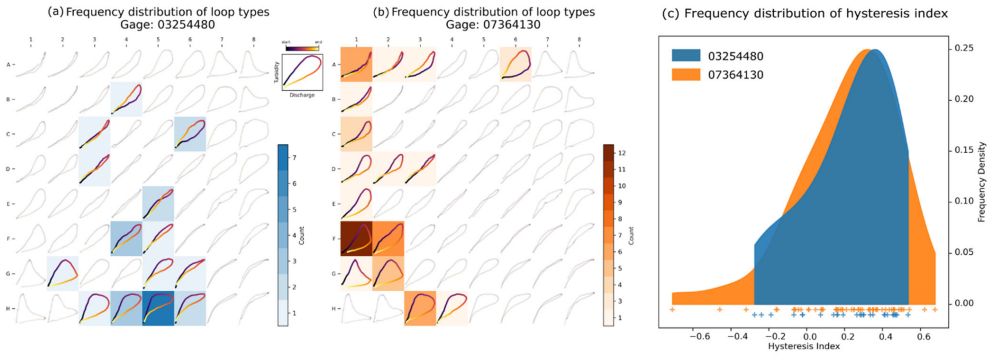

Figure 1~~2θ~~. Frequency distribution of loop types for watersheds 03254480 (~~1θ~~a) and 07364130 (~~1θ~~b) mapped onto the *General T-Q SOM* and the hysteresis index (~~1θ~~c). The frequency distributions mapped onto the *General T-Q SOM* reveal distinctions in loop types that are not captured by the hysteresis index.

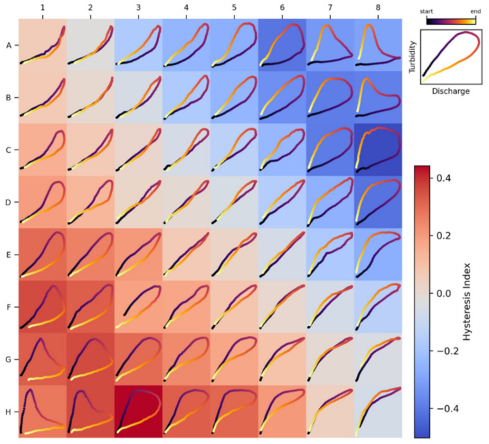

Figure 1~~1~~3. Distribution of hysteresis index values across the ~~*Kohonen map's*~~*General T-Q SOM.* ~~prototypes~~

Although a detailed analysis of the factors driving differences in loop types between watersheds 03254480 and 07364130 is beyond the scope of this ~~report~~technical note, the variations in frequency distribution displayed in Fig. 1~~0~~a and ~~10b~~ 12b likely reflect differences in sediment transport mechanisms. Concave-down loops are typically associated with significantly higher sediment concentrations during the falling limb of the hydrograph compared to concave-up loops (see Fig. 2; Williams (1989)). This could be the result of differences in the watersheds's physiographic attributes. Gage 03254480, located in northern Kentucky at the outlet of a 47~~.~~ km² watershed, is situated in hilly terrain with few flat areas (Mcgrain and Currens, 1978). In contrast, Gage 07364130, located in Arkansas at the outlet of a 311~~.~~ km² watershed, is characterized by low-relief topography dissected by meandering rivers and streams, typical of the alluvial plain of the Arkansas and Mississippi Rivers. The hydrologic regime of 07364130 is likely more base-flow dominated than that of 03254480, a condition that has been linked to the formation of concave-up loops in previous research (Bettel et al., 2025). While this explanation remains speculative and requires further analysis for validation, the *General T-Q SOM* proves valuable in identifying variations in hysteresis loops that might have been overlooked with traditional hysteresis indices.

4.2.2 Identifying associations between hydrologic variables and loop types

The relationship between loop types and associated variables is shown in Fig. 1~~4~~2~~,~~ as heatmaps of median values for rainfall (Fig. ~~12b~~14b), antecedent discharge (a proxy for antecedent moisture conditions; Fig. ~~12c~~14c), and the old-water to event-water ratio (a proxy for event flow pathways; Fig. ~~12d~~14d) for watershed 03289000. The heatmaps show clear relationships between loop types and hydrologic variables: precipitation increases from the upper-right to the lower-left corner of the map (Fig. 1~~4~~2b), linking higher precipitation to clockwise loops and lower precipitation to counterclockwise loops. Similarly, old-water to event-water ratios decrease along this same gradient, indicating a greater dominance of old-water contributions in counterclockwise loops compared to clockwise loops (Fig. 1~~4~~2d). In contrast, antecedent discharge values appear randomly distributed, showing no discernible pattern (Fig. 1~~4~~2c). These findings are consistent with our previous study (Marin-Ramirez et al., 2024), which identified rainfall and old-water to event-water ratios as key predictors of hysteresis variation, while antecedent conditions showed no significant association with the hysteresis patterns.

Fig. 1~~3~~54 complements this analysis by showing the quantitative relationship between loop types (as represented by BMU coordinates) and the hydrologic variables. The correlation analysis shown in Fig. 145~~3~~, as indicated by arrow lengths representing coefficients of determination ~~near 0.5~~, highlights the association between loop type and both precipitation and old-water to event-water ratios ($R^2 \sim 0.5$). In contrast, antecedent discharge shows negligible association, reflected in a near-zero coefficient and short arrow. The arrows reveal the direction of these associations: precipitation increases along the transition from counterclockwise to clockwise loops, while old-water to event-water ratios increase in the opposite direction. This supports the visual analysis shown in Fig. 14.

While verifying the causation of these relationships is outside the scope of this technical note ~~(and is explored more in~~ (and is explored more in Marin-Ramirez et al., 2024)~~)~~, we emphasize that the method provides a quantitative and repeatable approach for visualizing relationships between watershed variables and loop types, which overcomes limitations of traditional hysteresis anlayses.

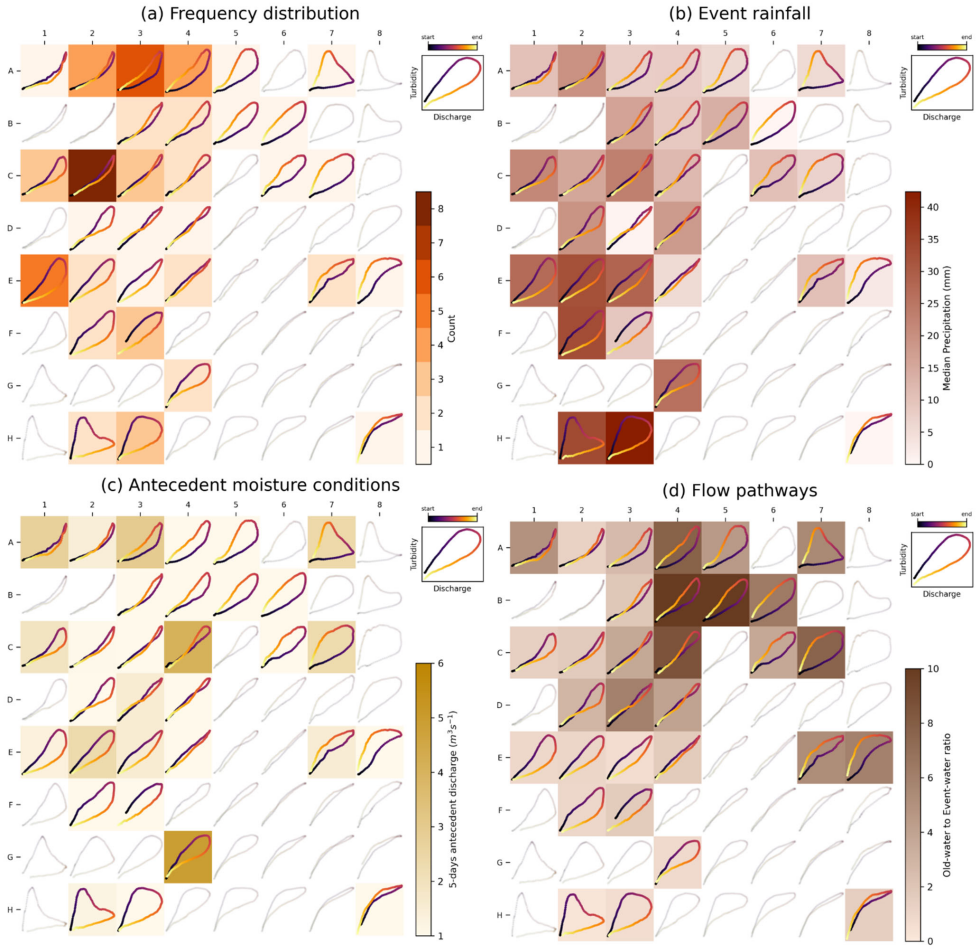

Figure 1~~2~~4. Heatmaps for watershed 03289000 of a) loop types, b) precipitation, c) antecedent discharge, and d) old-water to event-water ratio. The figure illustrates a visual approach for analyzing associations between hydrologic variables and loop types using the *General T-Q SOM*. In ~~Figs. 12~~panels b ~~-12e~~and c, the color intensity represents the median values of the variable calculated for loop samples mapped to each prototype. Consistent patterns are evident for precipitation (higher precipitation for clockwise loops) and the old-water to event-water ratio (higher ratios for counterclockwise loops), whereas no discernible pattern can be seen for the 5-day antecedent discharge.

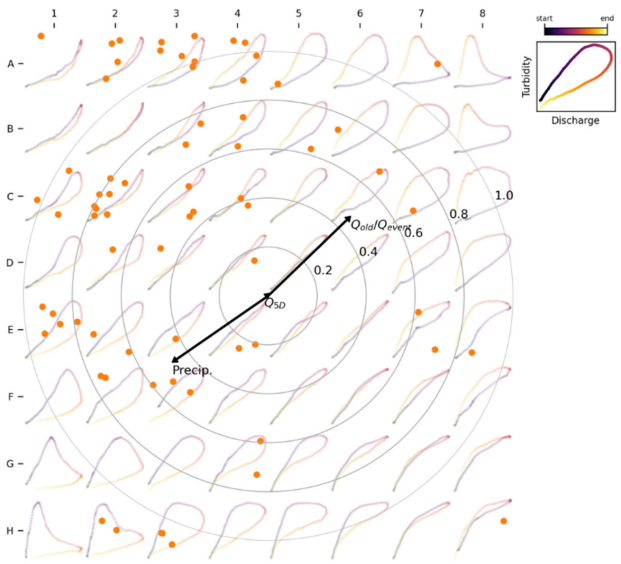

Figure 1~~3~~5. SOM-based biplot. The figure illustrates results from a correlation analysis between hysteresis loop types and hydrologic variables. The direction and length of the arrows are derived from multiple linear correlation analysis~~s~~, where BMU coordinates serve as the independent variables and the hydrologic variable~~s~~ ~~of interest~~ serve as the dependent variable~~s~~. Arrows indicate the direction of increasing variable values (e.g., precipitation increases for clockwise loops and decreases for counterclockwise loops). The length of each arrow corresponds to the coefficient of determination for the correlation, with reference values provided by the concentric circles. Each dot represents a sample loop, positioned randomly within the square circumscribed by its respective BMU.

5 Discussion

5.1 Efficacy of the SOM algorithm for C-Q analyses

In this technical note, we introduce a novel approach for characterizing C-Q hysteresis loops using the unsupervised machine learning algorithm, Self-Organizing Maps (SOM). ML has recently proven useful in hysteresis analysis, as demonstrated by Hamshaw et al. (2018), however the application of the SOM algorithm for hysteresis classification overcomes issues associated with classification of hysteresis loops to nominal categories. ~~While Hamshaw et al. (2018) previously proposed a machine learning-based method for classifying hysteresis loops, their approach closely mirrors manual classification by assigning loops to nominal categories.~~ As discussed in this study, such methods overlook the continuum of hysteresis loop variability by imposing arbitrary boundaries on loop classifications, disregarding the nuanced similarities and differences between loop types (see Fig. 1). In contrast, the SOM-based approach presented here preserves the gradual transitions between hysteresis ~~classes~~types, providing a more robust framework for exploring the hydrologic significance of diverse loop types ~~(Fig. 7)~~.

Formatted: Space Before: 0 pt, Line spacing: Multiple 1.15 li

Formatted: Heading 2

Formatted: Space After: 12 pt, Line spacing: Multiple 1.15 li

Our method also addresses key limitations inherent to hysteresis index-based approaches, which simplify loop shape variability into a single dimension (e.g., clockwise vs. counterclockwise). By contrast, SOMs offer a two-dimensional framework that enables ~~a more~~more nuanced discrimination of loop types while maintaining low dimensionality to facilitate further analyses, including visualization (see Figs. 1~~0~~2, ~~12~~14, and ~~13~~15). Moreover, the flexibility of this approach allows for extensions into higher dimensions, making it adaptable to the specific requirements of diverse applications.

By applying SOM to a curated dataset of ~~sediment transport~~ hysteresis loops, representative of sediment transport ~~sediment hysteresis types~~patterns ~~surveyed from the~~documented in the literature, we developed the *General T-Q SOM*. Beyond the advantages over nominal classification schemes, this map also improves upon hysteresis indices by capturing changes in concavity, which is ~~a feature~~ entirely overlooked by traditional hysteresis indices ~~(e.g.,~~ (e.g., Zuecco et al., 2016)~~)~~. ~~While loop concavity has historically received less attention in hysteresis analysis, p~~Previous studies highlight ~~its~~ the importance of concavity in characterizing C-Q relationships. ~~While~~ Williams (1989) first described concave up and concave down loops, while Evans and Davies (1998) demonstrated how relative contributions from different flow pathways shape distinct concavity patterns, suggesting concavity as an indicator of constituent sources. Bettel et al. (2025) further reinforced this concept, associating concave up loops with higher base flow contributions. These findings underscore the importance of concavity in understanding C-Q dynamics (see also Fig. 2) and highlight the *General T-Q SOM*'s value in supporting hysteresis workflows, particularly for identifying critical sources and pathways of sediment transport.

5.2 Future use of the SOM algorithm for C-Q analyses

Formatted: Heading 2

By offering an improved characterization of the spectrum of sediment hysteresis loop types ~~observed in watersheds~~, we believe the SOM algorithm will ~~has the potential to deepen~~enhance our understanding of the factors driving their emergence ~~of varying loop types, including hydrological variables and watershed structural properties~~, as ~~demonstrated~~ illustrated here with the *General T-Q SOM*. Scaling this analysis across watersheds with diverse physiographic conditions ~~is expected to provide~~can may yield valuable insights into the links between loop types~~, sediment sources, and transport pathways.~~, hydrologic conditions, and watershed characteristics ~~offering critical information to mitigate the negative impacts of excessive sediment transport~~. For example, trained SOMs can be further used to explore seasonal variations in sediment hysteresis within individual watersheds, such as contrasts between wet and dry seasons. Furthermore, the SOM algorithm can support regional or continental-scale characterizations of hysteresis behaviors, enabling comparison of hysteresis patterns across climate zones (e.g., arid and humid basins), as well as different physiographic settings (e.g., flat and steep basins)~~.~~; which, ~~U~~ultimately, ~~offering~~ may offer critical information to mitigate the negative impacts of excessive sediment transport.

Formatted: Space After: 12 pt, Line spacing: Multiple 1.15 li

While the *General T-Q SOM* (Fig. 9~~7~~) derived herein was created as a proof-of-concept of applying the SOM algorithm for hysteresis analyses, the map can readily be used for sediment transport hysteresis workflows more broadly. We demonstrate how this can be done by using data from three watersheds that were not utilized during the map training process. Importantly, for these watersheds, it was unnecessary to retrain the *General T-Q SOM* to facilitate the analysis. This trained model is included in the *HySOM* Python package released with this technical note (~~S~~see ~~S~~section 7).

Formatted: Font: Italic

However, studies examining less-common loop patterns or focused on specific loop features may require training alternative T-Q SOMs. For example, *Figure ~~8~~ eight* loops cannot be reliably distinguished from non-*figure ~~8~~ eight* loops with similar amplitude and concavity by the *General T-Q SOM* ~~derived herein~~ (see Fig. 10~~8~~). Attempts to improve the representation of *Figure ~~eight 8~~* loops (not shown) revealed that including this typology often resulted in highly distorted maps, which compromised the topological structure and disrupted smooth transitions between loop types. We suspect that three- or higher-

Formatted: Font: Italic

dimensional SOMs would be a suitable approach for incorporating *figure-eight* and other loop types while preserving a coherent topological structure in the map. We encourage researchers to explore this alternative.

Furthermore, how to incorporate ~~complex~~ irregular and less common loops (e.g.~~:~~, watershed-specific loop patterns not represented in the *General T-Q SOM*) ~~loops~~ into the SOM framework remains a~~-~~n open area of research~~challenge~~. ~~Complex loops do not have repeatable and consistent patterns that can readily be grouped to a single hysteresis prototype.~~

Addressing thi~~se~~ challenge~~s~~, initially, requires identification of loop types that do not fit well with the *General T-Q SOM*.

To ~~determine~~ identify these events, we propose that two approaches may be employed. For small datasets, visual inspection is recommended to flag loops that deviate fundamentally from those in the *General T-Q SOM*. This process can leverage the prototype arrangement within the *General T-Q SOM* to generate a structured visualization of the dataset, as illustrated in the supplementary material (Fig. S~~5~~2). Flagged loops can then be analyzed as an additional category, or the ~~*map*~~ *General T-Q SOM* could be retrained by incorporating the additional loop type in the training dataset. For larger datasets, where visualization of the entire dataset is impractical, outlier detection methods can be easily implemented for SOMs, for example, by comparing the QE of individual samples with the distribution of QEs for their associated prototypes, as proposed by Munoz and Muruzábal (1998). Interestingly, identified outliers may serve as candidates for training additional SOMs, aiding in the discovery of novel hysteresis patterns. We encourage researchers to use the *General T-Q* ~~*Map*~~ *SOM* as an initial benchmark and point of comparison to aid with uncovering such patterns in future analyses, thereby facilitating new understanding of the controls of sediment transport in watersheds.

While we chose to curate a dataset containing representative sediment hysteresis patterns for training the *General T-Q* SOM, alternative ~~uses~~methods to train hysteresis ~~of~~ SOMs are worth exploring. For example, training on large, uncurated datasets can serve as a powerful exploratory tool, leveraging SOM's visualization strengths to uncover dominant or previously unnoticed loop patterns. Note, however, that less frequent patterns may not be properly captured in the trained SOM due to the learning algorithm's limited exposure to rare types during training~~t~~ (Douzas and Bacao, 2017). Further research is encouraged to develop workflows that better identify and incorporate rare loop types with hydrological relevance.~~Ultimately we chose to use the curated dataset for training because: (i) it represents the known hysteresis loops for a given constituent, thereby ensuring broad applicability of the resulting SOM; (ii) guarantees representation of less frequent patterns; and (iii) provides a reference for evaluating the SOM's ability to distinguish loops in line with conceptual classifications. We viewed the third point as especially important for this technical note because SOM has never been applied to water quality hysteresis loops (to our knowledge) and therefore its efficacy for characterizing hysteresis loops needed to be tested.~~

Similarly, training an SOM on loops from a single watershed may reveal site-specific dynamics and deviations from the *General T-Q SOM*, offering valuable insights into local hysteresis behavior. However, such watershed-specific SOMs limit comparability across sites, as their prototypes are tailored to a single watershed. Additionally, if the number of available samples is small, the SOM may not be adequately trained, reducing its ability to capture meaningful structure in the hysteresis data.

~~Many additional analyses can be facilitated by applying the SOM algorithm to hysteresis patterns. For example, the SOM algorithm can facilitate investigation into seasonal variations in sediment hysteresis patterns in individual watersheds, such as~~

Formatted: Font: Italic

Formatted: Font: Italic

Formatted: Font: Italic

~~differences between wet and dry seasons. Furthermore, the SOM algorithm can support regional or continental-scale characterizations of hysteresis behaviors, enabling comparison of hysteresis patterns across climate zones (e.g., arid and humid basins), as well as different physiographic settings (e.g., flat and steep basins).~~

More broadly, we advocate for developing and carrying out analyses for SOMs tailored to other dissolved and suspended constituents, as distinct loop patterns are likely to emerge for different parameters. For instance, dissolved solids often exhibit dilution during hydrologic events, resulting in loops with a negative overall slope—a pattern rarely seen in sediment transport. To better capture these unique characteristics and understand their controls, we recommend creating C-Q SOM maps for other water quality parameters, such as nutrients, organic carbon, metals, and more. Additionally, researchers may find that distance functions other than DTW better capture hysteresis patterns for certain constituents, and we encourage exploration of such alternatives.

6 Conclusions

This study introduces a novel method for characterizing C-Q hysteresis loops using the Self-Organizing Map (SOM) algorithm. Unlike traditional classification schemes that rely on nominal categories and fail to account for the gradual variability among loop types, the SOM-based framework captures the ~~full~~ continuum of hysteresis loop variability. Furthermore, it addresses limitations of hysteresis indices by providing a two-dimensional representation that captures greater detail in loop shapes, offering a more nuanced depiction of the diversity within hysteresis loop types.

Our proof-of-concept application of the SOM algorithm for turbidity-discharge data demonstrates its efficacy for capturing key features of sediment hysteresis loops. This enabled the development of a *General T-Q SOM*, which ~~captures~~ represents the primary loop types associated with sediment transport hysteresis patterns. This map characterizes variations in rotational direction, loop amplitude, and, unlike traditional hysteresis indices, loop concavity. The inclusion of concavity adds a critical dimension to hysteresis analysis, as it has been linked to the dominance of different flow pathways, reflecting, along with the rotational direction, the relative contributions of different water and sediment sources. Alternative T-Q SOMs could be developed to better capture loop types not represented by the *General T-Q SOM*, such as *Figure ~~eight~~* loops or other uncommon patterns. We encourage use of the *General T-Q SOM* as a benchmark for future studies to facilitate discovery of novel hysteresis patterns.

We demonstrate how the *General T-Q SOM* can be used to facilitate workflows for hysteresis analysis. For example, we show how the map can be used to visualize hysteresis frequency distributions, facilitate hysteresis comparisons between watersheds, and link hydrologic processes to hysteresis patterns.

Finally, we discuss several promising avenues for application of the SOM algorithm for hysteresis analysis, including discerning seasonality of hysteresis patterns in individual watersheds, and, more broadly, applying the algorithm to characterize hysteresis behavior at the regional or continental scale. We advocate for the development of SOMs tailored to other dissolved and suspended constituents, as distinct loop patterns are likely to emerge for different parameters.

7 Code and data availability

We have released a Python package (https://github.com/ArlexMR/HySOM), designed to facilitate sediment transport hysteresis analysis ~~using the *General T-Q SOM* and train new SOMs for other constituents~~. The package includes the trained *General T-Q* SOM and ~~its original~~ the original *T-Q* ~~training dataset~~data used ~~to train the *General T-Q SOM*~~for its development.

Formatted: Line spacing: Multiple 1.15 li

Formatted: Space After: 0 pt, Line spacing: Multiple 1.15

Formatted: Space Before: 0 pt, Line spacing: Multiple 1.15 li

Formatted: Space After: 12 pt, Line spacing: Multiple 1.15 li

Formatted: Space Before: 0 pt, Line spacing: Multiple 1.15 li

Formatted: Space After: 12 pt, Line spacing: Multiple 1.15 li

Formatted: Font: Italic

Formatted: Font: Italic

, along with tools to train new SOM maps for other constituents. The package containsIt also provides functions for visualizing frequency distributions of hysteresis patterns mapped to a predefined SOM, similar to those included in this manuscript (Figs. 9, 12, and 14). Users are required to curate and input their own *CT-Q* hysteresis data for a given catchment, and wFe have included functions for preprocessing input data into the format required by the algorithm are also provided *HySOM* package (as shown in Fig. 7). Finally, We have also included functions in *HySOM* provides the training algorithm to generate new SOMs for precompiled hysteresis datasets (see *Training Phase* of Fig. 3). The user would be expected to provide these precompiled datasets, and we encourage users to follow our methods described in section 3.1 to do so.

8 Author contribution

Marin-RamirezAMR: conceptualization, data curation, formal analysis, investigation, methodology, software, supervision, visualization, writing (original draft preparation)

MahoneyDM: conceptualization, investigation, funding acquisition, investigation, methodology, project administration, resources, software, supervision, validation, visualization, writing (original draft preparation)

GMMcDaniel: conceptualization, data curation, formal analysis, writing (original draft preparation)

9 Competing interests

The authors declare that they have no conflict of interest.

10 Acknowledgements

We gratefully acknowledge the financial support of this research from the US Department of Transportation University Transportation Centers Program Award #69A3552348335, National Science Foundation Award #2217685: *The Inclusive Mentoring Hub in Kentucky and West Virginia*, and National Science Foundation Award #2418789: *The Flooding in Appalachian Streams and Headwaters (FLASH) Initiative.* We would like to thank our collaborators at the University of Kentucky for allowing us to access the turbidity data collected nearby USGS gage 03289000 used in this study.

11 References

Attik, M., Bougrain, L., and Alexandre, F.: Self-organizing map initialization, International Conference on Artificial Neural Networks, 357-362,

Bettel, L., Fox, J., Husic, A., Mahoney, T., Marin-Ramirez, A., Zhu, J., Tobin, B., Al-Aamery, N., Osborne, C., Riddle, B., and Pollock, E.: Hydrologic pathways and baseflow contributions, and not the proximity of sediment sources, determine the shape of sediment hysteresis curves: Theory development and application in a karst basin in Kentucky USA, Journal of Hydrology, 649, 132300, 10.1016/j.jhydrol.2024.132300, 2025.

Céréghino, R. and Park, Y. S.: Review of the Self-Organizing Map (SOM) approach in water resources: Commentary, Environmental Modelling & Software, 24, 945-947, 10.1016/j.envsoft.2009.01.008, 2009.

Chaney, N. W., Minasny, B., Herman, J. D., Nauman, T. W., Brungard, C. W., Morgan, C. L., McBratney, A. B., Wood, E. F., and Yimam, Y.: POLARIS soil properties: 30-m probabilistic maps of soil properties over the contiguous United States, Water Resources Research, 55, 2916-2938, 2019.

Clark, S., Sisson, S. A., and Sharma, A.: Tools for enhancing the application of self-organizing maps in water resources research and engineering, Advances in Water Resources, 143, 103676, 10.1016/j.advwatres.2020.103676, 2020.

Formatted: Space Before: 0 pt, Line spacing: Multiple 1.15 li

Formatted: Space After: 12 pt, Line spacing: Multiple 1.15 li

Formatted: Space Before: 0 pt, Line spacing: Multiple 1.15 li

Formatted: Space After: 12 pt, Line spacing: Multiple 1.15 li

Formatted: Space Before: 0 pt, Line spacing: Multiple 1.15 li

Formatted: Space After: 12 pt, Line spacing: Multiple 1.15 li

Formatted: Space Before: 0 pt, Line spacing: Multiple 1.15 li

Ding, H., Trajcevski, G., Scheuermann, P., Wang, X. Y., and Keogh, E.: Querying and Mining of Time Series Data: Experimental Comparison of Representations and Distance Measures, Proceedings of the Vldb Endowment, 1, 1542-1552, https://doi.org/10.14778/1454159.1454226, 2008.
Douzas, G. and Bacao, F.: Self-Organizing Map Oversampling (SOMO) for imbalanced data set learning, Expert systems with Applications, 82, 40-52, 2017.
Dupas, R., Tavenard, R., Fovet, O., Gilliet, N., Grimaldi, C., and Gascuel-Odoux, C.: Identifying seasonal patterns of phosphorus storm dynamics with dynamic time warping, Water Resources Research, 51, 8868-8882, 10.1002/2015wr017338, 2015.
Evans, C. and Davies, T. D.: Causes of concentration/discharge hysteresis and its potential as a tool for analysis of episode hydrochemistry, Water Resources Research, 34, 129-137, 10.1029/97wr01881, 1998.
Gellis, A. C.: Factors influencing storm-generated suspended-sediment concentrations and loads in four basins of contrasting land use, humid-tropical Puerto Rico, Catena, 104, 39-57, 10.1016/j.catena.2012.10.018, 2013.
Haddadchi, A. and Hicks, M.: Interpreting event-based suspended sediment concentration and flow hysteresis patterns, Journal of Soils and Sediments, 21, 592-612, 10.1007/s11368-020-02777-y, 2021.
Hamshaw, S. D., Dewoolkar, M. M., Schroth, A. W., Wemple, B. C., and Rizzo, D. M.: A New Machine-Learning Approach for Classifying Hysteresis in Suspended-Sediment Discharge Relationships Using High-Frequency Monitoring Data, Water Resources Research, 54, 4040-4058, 10.1029/2017wr022238, 2018.
Harris, C. R., Millman, K. J., Van Der Walt, S. J., Gommers, R., Virtanen, P., Cournapeau, D., Wieser, E., Taylor, J., Berg, S., and Smith, N. J.: Array programming with NumPy, nature, 585, 357-362, 2020.
Heidel, S. G.: The progressive lag of sediment concentration with flood waves, Eos, Transactions American Geophysical Union, 37, 56-66, 1956.
Hodson, T., Hariharan, J., Black, S., and Horsburgh, J.: dataretrieval (Python): a Python package for discovering and retrieving water data available from US federal hydrologic web services [code], 10.5066/P94I5TX3, 2023.
Husic, A., Fox, J. F., Clare, E., Mahoney, T., and Zarnaghsh, A.: Nitrate Hysteresis as a Tool for Revealing Storm-Event Dynamics and Improving Water Quality Model Performance, Water Resources Research, 59, e2022WR033180, 10.1029/2022WR033180, 2023.
Jing, T. G., Zeng, Y., Fang, N. F., Dai, W., and Shi, Z. H.: A Review of Suspended Sediment Hysteresis, Water Resources Research, 61, e2024WR037216, 10.1029/2024WR037216, 2025.
Kalteh, A. M., Hiorth, P., and Bemdtsson, R.: Review of the self-organizing map (SOM) approach in water resources: Analysis, modelling and application, Environmental Modelling & Software, 23, 835-845, 10.1016/j.envsoft.2007.10.001, 2008.
Kiviluoto, K.: Topology preservation in self-organizing maps, Proceedings of International Conference on Neural Networks (ICNN'96), 294-299,
Kohonen, T.: Self-Organized Formation of Topologically Correct Feature Maps, Biological Cybernetics, 43, 59-69, 10.1007/Bf00337288, 1982.
Kohonen, T.: The self-organizing map, Proceedings of the IEEE, 78, 1464-1480, 1990.
Kohonen, T.: Essentials of the self-organizing map, Neural Netw, 37, 52-65, 10.1016/j.neunet.2012.09.018, 2013.
Koppa, A., Gebremichael, M., and Yeh, W. W.: Multivariate calibration of large scale hydrologic models: The necessity and value of a Pareto optimal approach, Advances in Water Resources, 130, 129-146, 2019.
Lee, S., Kim, J., Hwang, J., Lee, E., Lee, K. J., Oh, J., Park, J., and Heo, T. Y.: Clustering of Time Series Water Quality Data Using Dynamic Time Warping: A Case Study from the Bukhan River Water Quality Monitoring Network, Water, 12, 2411, 10.3390/w12092411, 2020.
Liu, W., Birgand, F., Tian, S., and Chen, C.: Event-scale hysteresis metrics to reveal processes and mechanisms controlling constituent export from watersheds: A review(☆), Water Res, 200, 117254, 10.1016/j.watres.2021.117254, 2021.
Lloyd, C. E. M., Freer, J. E., Johnes, P. J., and Collins, A. L.: Using hysteresis analysis of high-resolution water quality monitoring data, including uncertainty, to infer controls on nutrient and sediment transfer in catchments, Sci Total Environ, 543, 388-404, 10.1016/j.scitotenv.2015.11.028, 2016.
Malutta, S., Kobiyama, M., Chaffe, P. L. B., and Bonuma, N. B.: Hysteresis analysis to quantify and qualify the sediment dynamics: state of the art, Water Sci Technol, 81, 2471-2487, 10.2166/wst.2020.279, 2020.

Marin-Ramirez, A., Mahoney, D. T., Riddle, B., Bettel, L., and Fox, J. F.: Response time of fast flowing hydrologic pathways controls sediment hysteresis in a low-gradient watershed, as evidenced from tracer results and machine learning models, Journal of Hydrology, 645, 132207, 10.1016/j.jhydrol.2024.132207, 2024.

Mazilamani, L. S., Walsh, R. P. D., Annammala, K. V., Bidin, K., Yusop, Z., Reynolds, G., and Nainar, A.: Concentration-discharge hysteresis: current approaches and future directions for quantifying pollutant dynamics in storm events-with a particular focus on the tropics, Sustainable Water Resources Management, 10, 156, 10.1007/s40899-024-01130-2, 2024.

McGrain, P. and Currens, J. C.: Topography of Kentucky: Kentucky Geological Survey, Series X, Special Publication, 25, 76, 1978.

Miljković, D.: Brief review of self-organizing maps, 2017 40th international convention on information and communication technology, electronics and microelectronics (MIPRO), 1061-1066,

Molder, B., Cockburn, J., Berg, A., Lindsay, J., and Woodrow, K.: Sediment-assisted nutrient transfer from a small, no-till, tile drained watershed in Southwestern Ontario, Canada, Agricultural Water Management, 152, 31-40, 10.1016/j.agwat.2014.12.010, 2015.

Munoz, A. and Muruzábal, J.: Self-organizing maps for outlier detection, Neurocomputing, 18, 33-60, 1998.

Pickering, C. and Ford, W. I.: Effect of watershed disturbance and river-tributary confluences on watershed sedimentation dynamics in the Western Allegheny Plateau, Journal of Hydrology, 602, 126784, 10.1016/j.jhydrol.2021.126784, 2021.

Pölzlbauer, G.: Survey and comparison of quality measures for self-organizing maps, in: Proceedings of the Fifth Workshop on Data Analysis (WDA2004), edited by: Paralič, J., Pölzlbauer, G., and Rauber, A., Elfa Academic Press, 67-82, 2004.

Samarasinghe, S.: Neural networks for applied sciences and engineering: from fundamentals to complex pattern recognition, Auerbach publications2016.

Sherriff, S. C., Rowan, J. S., Fenton, O., Jordan, P., Melland, A. R., Mellander, P. E., and hUallachain, D. O.: Storm Event Suspended Sediment-Discharge Hysteresis and Controls in Agricultural Watersheds: Implications for Watershed Scale Sediment Management, Environ Sci Technol, 50, 1769-1778, 10.1021/acs.est.5b04573, 2016.

Shokoohi-Yekta, M., Hu, B., Jin, H., Wang, J., and Keogh, E.: Generalizing DTW to the multi-dimensional case requires an adaptive approach, Data Min Knowl Discov, 31, 1-31, 10.1007/s10618-016-0455-0, 2017.

Speir, S. L., Rose, L. A., Blaszczak, J. R., Kincaid, D. W., Fazekas, H. M., Webster, A. J., Wolford, M. A., Shogren, A. J., and Wymore, A. S.: Catchment concentration–discharge relationships across temporal scales: A review, Wiley Interdisciplinary Reviews: Water, 11, e1702, 10.1002/wat2.1702, 2024.

Tavenard, R., Faouzi, J., Vandewiele, G., Divo, F., Androz, G., Holtz, C., Payne, M., Yurchak, R., Rußwurm, M., and Kolar, K.: Tslearn, a machine learning toolkit for time series data, Journal of machine learning research, 21, 1-6, 2020.

Vesanto, J.: Neural network tool for data mining: SOM toolbox, Proceedings of symposium on tool environments and development methods for intelligent systems (TOOLMET2000), 184-196,

Williams, G. P.: Sediment Concentration Versus Water Discharge during Single Hydrologic Events in Rivers, Journal of Hydrology, 111, 89-106, 10.1016/0022-1694(89)90254-0, 1989.

Zarnaghsh, A. and Husic, A.: Degree of Anthropogenic Land Disturbance Controls Fluvial Sediment Hysteresis, Environ Sci Technol, 55, 13737-13748, 10.1021/acs.est.1c00740, 2021.

Zuecco, G., Penna, D., Borga, M., and van Meerveld, H. J.: A versatile index to characterize hysteresis between hydrological variables at the runoff event timescale, Hydrological Processes, 30, 1449-1466, 10.1002/hyp.10681, 2016.

Formatted: Line spacing: Multiple 1.15 li